Accepted for publication in ApJ
Preprint typeset using LaTeX style emulateapj v. 05/12/14

arXiv:1409.0016v2 [astro-ph.SR] 13 Apr 2015

WARM DUST AROUND COOL STARS: FIELD M DWARFS WITH *WISE* 12 OR 22 MICRON EXCESS EMISSION

Christopher A. Theissen and Andrew A. West
Department of Astronomy, Boston University, 725 Commonwealth Avenue, Boston, MA 02215, USA
Accepted for publication in ApJ

ABSTRACT

Using the SDSS DR7 spectroscopic catalog, we searched the *WISE* AllWISE catalog to investigate the occurrence of warm dust, as inferred from IR excesses, around field M dwarfs (dMs). We developed SDSS/*WISE* color selection criteria to identify 175 dMs (from 70,841) that show IR flux greater than typical dM photosphere levels at 12 and/or 22 μm, including seven new stars within the Orion OB1 footprint. We characterize the dust populations inferred from each IR excess, and investigate the possibility that these excesses could arise from ultracool binary companions by modeling combined SEDs. Our observed IR fluxes are greater than levels expected from ultracool companions ($> 3\sigma$). We also estimate that the probability the observed IR excesses are due to chance alignments with extragalactic sources is $< 0.1\%$. Using SDSS spectra we measure surface gravity dependent features (K, Na, and CaH 3), and find $< 15\%$ of our sample indicate low surface gravities. Examining tracers of youth (Hα, UV fluxes, and Li absorption), we find $< 3\%$ of our sample appear young, indicating we are observing a population of field stars $\gtrsim 1$ Gyr, likely harboring circumstellar material. We investigate age-dependent properties probed by this sample, studying the disk fraction as a function of Galactic height. The fraction remains small and constant to $|Z| \sim 700$ pc, and then drops, indicating little to no trend with age. Possible explanations for disks around field dMs include: 1) collisions of planetary bodies, 2) tidal disruption of planetary bodies, or 3) failed planet formation.

Keywords: circumstellar material — infrared: stars — planet-disk interactions — stars: low-mass

1. INTRODUCTION

Disks are an important part of stellar and planetary evolution, providing the building blocks for planetary systems around all types of stars. Since the discovery of a disk-like structure encircling the A0V star Vega (Aumann et al. 1984), the study of circumstellar disks has expanded our understanding of stellar and planetary evolution. After its launch in 1983, the *Infrared Astronomical Satellite* (*IRAS;* Neugebauer et al. 1984) observed an unprecedented number of young stellar objects (YSOs), in addition to more evolved stars, akin to Vega, which were identified by their excess infrared (IR) fluxes (Zuckerman 2001). For the first time, a diverse range of disks were characterized by their IR signatures (Lada 1987), from pre-main sequence stars showing near-IR (NIR) excesses due to a hot shell of infalling material, to colder disks analogous to the Kuiper belt, showing far-IR (FIR) excess fluxes (e.g., Vega; Su et al. 2005). The *Spitzer Space Telescope* (Werner et al. 2004), launched in 2003, allowed for further characterization of disk populations, categorizing the transitional disk phase (Espaillat et al. 2014), where IR gaps appear as signposts of planetary construction. The high sensitivity and long wavelength range (from 10^{-4} mJy at 3.6 μm to 10 mJy at 160 μm) of *Spitzer* allowed for some of the most detailed studies of nearby star-forming regions to date (Williams & Cieza 2011, and references therein).

As a successor to *Spitzer*, *Herschel* (Pilbratt et al. 2010) was able to probe even colder disk populations, with spectral energy distributions (SEDs) peaking between 55–670 μm, and at an unprecedented resolution. Studies using *Herschel* have investigated the properties of cold debris disks (Eiroa et al. 2010; Greaves 2010; Acke et al. 2012; Eiroa et al. 2013). *Herschel* was also able to measure a new class of cold debris disks, with temperatures of $\sim$22 K (Eiroa et al. 2011; Ertel et al. 2012; Krivov et al. 2013). Although there is still some debate on whether these observed FIR excesses originate from cold circumstellar material versus Galactic contamination (Gáspár & Rieke 2014), their existence demonstrates the sensitivity of *Herschel*.

While *Spitzer* and *Herschel* provided targeted IR observations, much of the sky remained void of IR observations. In 2011, The *Wide-field Infrared Survey Explorer* (*WISE*; Wright et al. 2010) completed an all-sky IR survey, providing the ability to study the IR properties of field stars that are not members of stellar associations or young star-forming regions. The *WISE* observational strategy allows for a "blind" search for stars exhibiting IR excesses above their photospheres across the sky. *WISE* observations are currently helping to answer stellar and planetary evolution questions regarding the mechanisms responsible for disk dispersal, the detailed timescales on which they act, and how they differ with stellar mass (e.g., Avenhaus et al. 2012; Heng & Malik 2013).

M dwarfs, being the most populous ($\sim$70% of the stellar population; Bochanski et al. 2010) and longest living stellar constituents (main sequence lifetimes $\sim 10^{12}$ yrs; Laughlin et al. 1997), offer a laboratory in which to study the statistical properties of our Galaxy. In addition, recent studies have shown that M dwarfs have high probabilities of harboring Earth-sized terrestrial planets (Howard et al. 2012; Swift et al. 2012; Dressing & Charbonneau 2013), allowing studies to constrain the number of planetary systems within the Milky

ctheisse@bu.edu

Way. However, despite huge advances in the study of circumstellar material over the past decade, the detailed process of planetary formation around low-mass stars ($\lesssim 0.6 M_{\odot}$) still elicits questions regarding the mass-dependence of circumstellar disk evolution.

The earliest investigations of disks around low-mass stars used *IRAS* to detect signatures of cold dust (< 100 K) by identifying small 25 μm excesses around stars in young star-forming regions. Many of these detections were found to be false-positives (Zuckerman 2001; Song et al. 2002; Plavchan et al. 2005), possibly due to the low spatial resolution of *IRAS* and consequent blending of background sources with target sources, or a detection threshold bias, leaving a dearth of low-mass stars with cold disks. One such study undertaken by Plavchan et al. (2005) investigated the paucity of cold disks around M dwarfs, using small mid-IR (MIR) excesses (> 10 μm) as a proxy, and postulated that rapid planet formation (Weinberger et al. 2004; Boss 2006) may be a cause for the dearth of cold disks around low-mass stars older than 10 Myr. However, recent studies have suggested that this deficiency is likely due to *IRAS* detection limits (Forbrich et al. 2008; Plavchan et al. 2009).

Forbrich et al. (2008) used the *Spitzer* Multiband Imaging Photometer (MIPS; 24, 70, and 160 μm bands) to study NGC 2547, a cluster with an age of 30–40 Myr, and specifically targeted low-mass stars within the region. Using the FIR abilities of *Spitzer*, Forbrich et al. (2008) were able to increase the number of known M dwarfs with cold disks from six to fifteen, as inferred from their 24 μm excesses. In addition, Plavchan et al. (2009) completed *Spitzer* observations of 70 main sequence stars between ages of 8 Myr to 1.1 Gyr and found that small 24 μm excesses ($\sim$10% above the expected photospheric flux), associated with cold disks, were common around young stars of all spectral types. Plavchan et al. (2009) also observed that large 70 μm excesses ($\gg 100\%$ above the expected photospheric flux) were more common around stars with $T_* > 5{,}000$ K in the 200–500 Myr range than stars with $T_* < 5{,}000$ K in the 8–50 Myr range. The discrepancy in 70 μm excesses may be due to higher-mass stars having larger, brighter photospheres, irradiating a larger portion of the disk. It is also probable that disks around higher mass stars are more massive due to the larger protostellar envelope from which they are formed (Plavchan et al. 2009). Another important consideration is observations at a specific wavelength probe different sections of the disk for different stellar temperatures (Kennedy & Kenyon 2009). The number of M dwarfs showing signs of dust is currently insufficient to properly address the questions of disk evolution and structure for the lowest mass stars.

The excess differences between hot and cool main sequence stars found by Plavchan et al. (2009) can be explained by invoking mass-dependent evolution of circumstellar disks. Several studies have found that young star-forming regions (< 5 Myr) show drastically different fractions of stars exhibiting IR excesses above their photospheres as a function of spectral type (Carpenter et al. 2006; Lada et al. 2006; Luhman et al. 2008; Carpenter et al. 2009; Luhman et al. 2010). Even regions of approximately similar ages showed significant differences in their disk fractions, possibly as a result of the density of stars within the region (e.g., open versus globular clusters; Luhman et al. 2008, 2010). Other studies have pointed to metallicity playing a significant role in circumstellar disk evolution (Yasui et al. 2009, 2010). The planet-metallicity correlation (Gonzalez 1997; Laws et al. 2003; Fischer & Valenti 2005; Johnson et al. 2010; Rojas-Ayala et al. 2010) may imply that rapid formation of planets in these higher metallicity systems, could disperse the disk on faster timescales. These effects may be significant for M dwarfs, which are prone to low-mass planet formation (Swift et al. 2012; Dressing & Charbonneau 2013). However, other studies have suggested that stellar metallicity does not correlate with the occurrence of Earth-sized terrestrial planets (Mayor et al. 2011; Buchhave et al. 2012). Observations indicate that Earth-sized planets appear to be more common around M dwarfs than Jupiter-sized planets, suggestive that metallicity may not play a significant role in planet formation for the lowest-mass stars (Dressing & Charbonneau 2013). The link between metallicity, planet formation, and disk evolution around low-mass stars still requires further investigation.

In recent years, a new class of older stars ($\gtrsim 1$ Gyr) exhibiting IR excess has been identified (Rhee et al. 2008; Moór et al. 2009; Fujiwara et al. 2010; Melis et al. 2010b; Weinberger et al. 2011). These solar-type stars (FGK-spectral types) pose questions regarding our current understanding of disk evolution. One such star, BD +20 307, investigated by Weinberger et al. (2011) was found to have a large IR excess ($L_{IR}/L_* \approx 10^{-2}$), speculated to have been caused by the collision of two planetary-sized bodies within the terrestrial zone. Such a phenomenon has not been observed around M dwarfs, presumably due to their intrinsic faintness coupled with the sensitivity limits of previous IR surveys (e.g., *IRAS*). However, due to the extremely long lifetimes of M dwarfs ($\sim 10^{12}$ yrs), these stars give us the ability to study the long-term stability of planetary systems, and other possible evolutionary scenarios such as 2$^{\rm nd}$ generation planet formation (Melis et al. 2009, 2010a; Perets 2010).

One strategy to increase source detections, and hence statistics, is to increase the solid angle of sky surveyed and the spectral coverage of observations. With the advent of large-area and all-sky surveys, the capability to study statistically significant populations of field stars has recently become available. At optical wavelengths, the Sloan Digital Sky Survey (SDSS; York et al. 2000) has become invaluable in creating large catalogs of low-mass stars (Bochanski et al. 2010; West et al. 2011). In the NIR, the Two Micron All-Sky Survey (2MASS; Skrutskie et al. 2006) has been extremely useful in discovering hot dust populations ($> 1{,}000$ K), making up the "pre-transitional" disk phase of protostellar evolution (Espaillat et al. 2014). The *WISE* mission recently completed an all-sky survey in the MIR. The all-sky nature and depth of *WISE* has made it possible to search for stars that exhibit infrared excesses and are not in young star-forming regions (e.g., Avenhaus et al. 2012; Kennedy & Wyatt 2012). Together, SDSS, 2MASS, and now *WISE* provide photometric coverage over an extremely large solid-angle of sky, from the optical to MIR. These surveys have given astronomers the ability to search for low-mass objects in young star-forming

regions (Dawson et al. 2012) and nearby young moving groups (NYMGs; Shkolnik et al. 2011), study the statistical properties of our Galaxy (Bochanski 2008; Bochanski et al. 2010; West et al. 2008, 2011), and explore the optical and IR properties of vast numbers of sub-solar objects (Hawley et al. 2002; Kirkpatrick et al. 2011). 2MASS and *WISE* are useful in constraining the effective temperature for low-mass stars, since their SEDs peak and turn over in the NIR.

A difficulty in searching for new, young, low-mass stars is the uncertainty in determining stellar ages. Many different methods are used to estimate ages for stars, including: 1) determining the lithium depletion boundary (Cargile et al. 2010); 2) using spectroscopic tracers such as sodium (Schlieder et al. 2012a) and Hα (West et al. 2008, 2011); 3) rotation and activity (Mohanty & Basri 2003; Reiners & Basri 2008); and 4) ultraviolet flux (Shkolnik et al. 2011; Schlieder et al. 2012b). Each of these youth indicators has its caveats, including the fact that metallicity may affect lithium equivalent width measurements (Pinsonneault 1997), or binarity may affect rotation and activity (Morgan et al. 2012). As such, it is important to test for multiple tracers of youth to definitively classify a star as young ($\lesssim$ 100 Myr) versus old ($\gtrsim$ 1 Gyr). Age is an important parameter for stars exhibiting IR excess as it potentially helps to differentiate stars harboring primordial dust from 2$^{\rm nd}$ generation scenarios that create circumstellar material.

A limitation in the search for disks around low-mass stars has been the lack of a reliable input catalog. Widely used stellar catalogs have been biased towards bluer stars, due to the intrinsic faintness of M dwarfs and blue bias of previous filters (e.g., *Hipparcos*, Tycho-2, etc.) This study aims to increase the number of known M dwarfs with MIR excesses by combining data from SDSS, 2MASS, and *WISE*. We searched the *WISE* AllWISE source catalog for signs of IR excess around the M dwarf spectroscopic sample of West et al. (70,841 M dwarfs; 2011). In §2 we outline our selection criteria for high-probability disk candidates from the sample compiled by West et al. (2011), define SDSS and *WISE* color-color criteria for selecting M dwarfs with IR excesses, and address the issue of interstellar reddening. Combining SDSS, 2MASS, and *WISE* photometry, we create SEDs for our candidates in §3, and explore the possibility that our IR excesses could be due to an ultracool companion, Galactic IR cirrus, or extragalactic contamination. In §4 we characterize our stars and observed dust content by: 1) modeling the dust populations using idealized parameters (§4.1), and 2) investigating a number of tracers for activity, surface gravity, and accretion as proxies for youth (§4.2). We also briefly discuss stars of interest at the end of §4. A discussion of our sample and possible interpretations and scenarios for circumstellar material around field dwarfs follows in §5. Lastly, in §6 we summarize our findings.

2. DATA

To construct SEDs and identify stars with excess IR flux requires data over a large wavelength regime, from the optical to the MIR. Additionally, spectroscopic data can be used to determine stellar parameters (§3) and youth diagnostics (§4.2). To obtain data over the wavelength coverage needed, we combined data sets from SDSS, 2MASS, and *WISE*.

SDSS has played an integral role in the statistical study of large stellar populations, specifically low-mass stars. The magnitude limits of SDSS allow the survey to probe M dwarfs out to distances > 1,000 pc, yielding vast photometric catalogs of M dwarfs (> 30 million; Bochanski et al. 2010). In addition, the medium resolution ($R \approx 1{,}800$) spectroscopic pipeline for SDSS has produced prodigious spectroscopic samples of M dwarfs (West et al. 2008, 2011, hereafter W08, W11, respectively). W11 used SDSS Data Release 7 (DR7; Abazajian et al. 2009) to compile a spectroscopic catalog of 70,841 M dwarfs. All of the stars were visually spectral typed using the Hammer IDL routine (Covey et al. 2007). We also measured radial velocities (RVs) using a cross-correlation-like program, a Python version of the `xcorl.pro` IDL procedure (Mohanty & Basri 2003; West & Basri 2009), comparing each spectrum with the appropriate M dwarf template (Bochanski et al. 2007b). This method yields typical uncertainties of $\sim$7 km s^{-1} (Bochanski et al. 2007b).

NIR and MIR data were obtained from the 2MASS point source catalog (Skrutskie et al. 2006) and *WISE* AllWISE source catalog (Wright et al. 2010; Mainzer et al. 2011), respectively. 2MASS provides full-sky coverage in three NIR bands (J: 1.25, H: 1.65, and K_s: 2.17 μm). The SEDs of M dwarfs peak in the NIR, thus, 2MASS photometry is especially critical in constraining the stellar effective temperature. In addition, 2MASS provides quality flags, useful to W11 in building the spectroscopic catalog and to this study, for ensuring point-source (GAL_CONTAM), high-quality photometry (RD_FLG & CC_FLAG). We required these quality flags for our own cuts outlined below.

In 2009, NASA launched *WISE* with the mission of completing an all-sky survey in four MIR bands (Wright et al. 2010). These bands were centered at 3.4, 4.6, 12, and 22 μm, hereafter referred to as $W1$, $W2$, $W3$, and $W4$, respectively. *WISE* is the most sensitive all-sky MIR survey to date, surpassing *IRAS*, and the recent survey completed by *AKARI* (Murakami et al. 2007) in 2007. $W1$, $W2$, $W3$, and $W4$ have angular resolutions of 6.1″, 6.4″, 6.5″, and 12″, and 5σ point source sensitivities of 0.068, 0.098, 0.86 and 5.4 mJy, respectively. *WISE* bands, specifically the 12 and 22 μm, probe the wavelength regime where warm ($T \sim$ 30–300 K) dust populations peak in the observed SED. The *WISE* photometric pipeline also provides a number of quality flags useful in selecting point sources including the contamination and confusion flag (CC_FLAG), and extended source flag (EXT_FLAG).

2.1. *Sample Selection*

Starting with the W11 catalog of 70,841 spectroscopically confirmed M dwarfs, we selected a sample of stars showing IR excesses above their photospheres starting with the following selection process (cuts 4, 5, and 6 were taken from the *WISE* Explanatory Supplement[1]; the number of stars left after each cut is given in parenthesis at the end of each selection criterion):

1. We matched the W11 catalog to the *WISE* All-

[1] http://wise2.ipac.caltech.edu/docs/release/allwise/expsup/sec2_2a.html

WISE source catalog[2], matching only to unique *WISE* counterparts within 5″. (66,890 stars)

2. The low angular resolution of *WISE* (FWHM = 6.1″, 6.4″, 6.5″, and 12″ in $W1$, $W2$, $W3$, and $W4$, respectively) required selection criteria to ensure that disk candidates were not contaminated by nearby sources. Using the SDSS-II CasJobs site[3] we obtained all DR7 primary photometric objects within 6″ of our stars (to match the $W4$ beam) and kept only stars did not have another primary photometric object within a 6″ radius. We applied the same criteria to stars with another 2MASS photometric object within 6″ (n_2mass < 2)[4]. (57,544 stars)

3. We required high-quality photometry from the optical through the NIR. To achieve this, we kept only stars with reliable SDSS photometry as determined in W11 (goodphot = 1[5]), and photometry in all three 2MASS bands. (43,253 stars)

4. We kept only stars with source morphology that was consistent with a single point-spread function (PSF) in *WISE* (ext_flag = 0). (42,892 stars)

5. Stars without a contamination and confusion flag in $W3$ (cc_flag = 0) were kept. This removed sources that could be due to diffraction spikes or scattered light from a nearby bright source. We did not require this for $W1$ or $W2$ since these bands were not used for our SED fitting, and we were most concerned with real excesses at 12 μm. (42,632 stars)

6. Stars that had a signal-to-noise (S/N) ratio (SNR) ≥ 3 in $W1$, $W2$, or $W3$ were included. Due to the distances to stars in the W11 catalog (100–2,000 pc), we expect real excesses to be faint, therefore we chose this S/N to be as inclusive as possible. An IR excess may also be observed in $W4$, however, as this was the shallowest *WISE* band, we did not require a minimum $W4$ S/N. We will discuss 22 μm excesses in our sample in §2.1.1. (2,698 stars)

7. Although the M giant contamination rate for the W11 catalog was estimated to be less than 0.5%, we removed potential dusty giants from our sample. Using the results from Bessell & Brett (1988) we assumed any star with a $J - H > 0.8$ has a significant probability of being an M giant. We kept stars: 1) that had $J - H \leq 0.8$; or 2) that had $J - H > 0.8$ and whose total USNO-B proper motions were greater than the total uncertainty ($\mu_{\rm tot} > \sigma_{\mu_{\rm tot}}$) and whose total proper motions were not zero ($\mu_{\rm tot} \neq 0$). (2,665 stars)

[2] http://irsa.ipac.caltech.edu/Missions/wise.html

[3] http://casjobs.sdss.org/CasJobs/

[4] Definitions for *WISE* flags can be found at http://wise2.ipac.caltech.edu/docs/release/allwise/expsup/sec2_1a.html

[5] Defined by SDSS photometric processing flags: SATURATED, PEAKCENTER, NOTCHECKED, PSF_FLUX_INTERP, INTERP_CENTER, BAD_COUNTS_ERROR set to zero in the r, i, and z bands.

These initial selection criteria reduced the sample size to 2,665 stars with reliable photometry in SDSS through $W3$ bands and no source confusion or contamination. We investigated other possible explanations for IR excesses around field dwarfs, specifically an ultracool companion or galactic/extragalactic contamination sources. We explore the likelihood of our IR excesses being attributable to these interlopers in §3.1 and §3.2, respectively.

2.1.1. *Identifying the Disk Candidates*

Avenhaus et al. (2012, hereafter A12) used low-mass stars from the RECONS 100 nearest star systems[6] (Jao et al. 2005; Henry et al. 2006) to search for MIR excesses around K and M dwarfs using *WISE*. This nearby sample offered high S/N *WISE* observations, as well as accurate parallax measurements and absolute magnitudes. Although A12 did not find any MIR excesses, presumably due to the older age of the nearby stellar sample ($\gtrsim$ 30 Myrs), they were able to determine typical MIR colors for K and M dwarfs. The A12 excess criteria require absolute magnitudes as a proxy for stellar effective temperature, hence distances are required. Our sample has photometric distances, with typical uncertainties of ∼20%, originally computed by W11 using the photometric parallax polynomials from Bochanski et al. (2010), and then dust-corrected by Jones et al. (2011), we use the dust-corrected of these distances in our analysis.

A12 defined their metric of IR excess significance as

$$\sigma' = \frac{e}{\sigma}\frac{1}{\sqrt{\chi^2}},$$

where e is the deviation from the A12 polynomial, σ is the *WISE* measurement error, and χ^2 is the overall goodness-of-fit for the A12 color-magnitude relationship. Using the M_{W1}-SpT excess criteria of A12, we found that 480 of the 2,665 stars from our initial cuts showed significant IR excess ($\geq 5\sigma'$) in their $W1-W3$ color, as shown in Figure 1. Visual inspection of these 480 stars in SDSS *gri* composite images[7] and spectra showed that 171 of the 480 candidate stars were contaminated by nearby galaxies or bright sources, or were misclassified, appearing spectroscopically as either galaxies or K dwarfs. This visual inspection left 309 remaining candidate stars. An example of stars kept versus stars that were removed due to contamination is shown in Figure 2.

One complication with using absolute magnitude as a temperature proxy is that pre-main sequence stars will appear as earlier spectral types (than their main sequence counterparts at the same mass) due to their larger photospheres. A12 discovered that $V - K_s$ was a much better discriminator for $T_{\rm eff}$. The SDSS, $r - z$ color has been shown to be a reliable proxy for stellar effective temperature (e.g., Bochanski et al. 2010, 2011). To overcome the limitations of using the A12 absolute magnitude polynomials, we examined $r - z$ color as a function of *WISE* colors for the 309 remaining stars in our sample, and the stars not exhibiting *WISE* excesses ($< 5\sigma'$). We computed $r - z$ polynomials, similar to the methods A12 used for $V - K_s$ color. In $r - z$ space, two

[6] http://www.chara.gsu.edu/RECONS/TOP100.posted.htm

[7] http://cas.sdss.org/dr7/en/tools/chart/list.asp

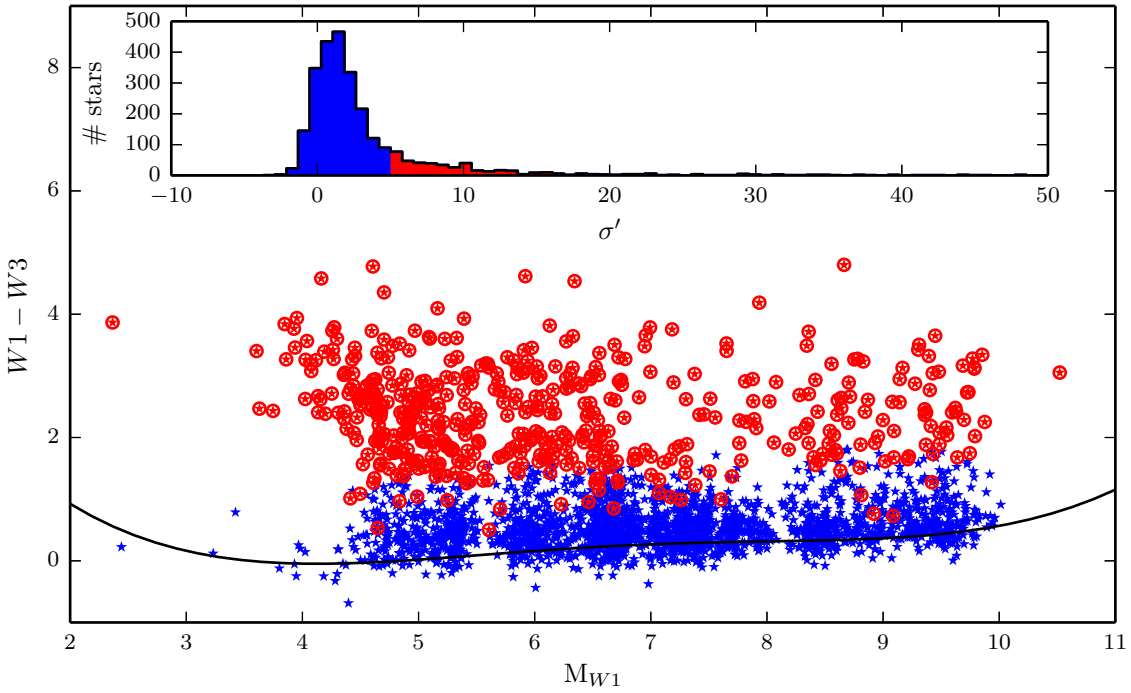

Figure 1. *WISE* Color-magnitude plot for the stars that made our initial cuts but prior to visual inspection (480 excess and 2,185 non-excess stars). The A12 polynomial is plotted (black line), along with the distribution of excess significance as determined by the A12 criteria. Stars $\geq 5\sigma'$ (defined in A12) are plotted as red stars with circles, representing the disk candidates. Stars below the $5\sigma'$ limit are plotted in blue stars. The overlap region is due to excess candidates ($\geq 5\sigma'$) with small *WISE* measurement uncertainties, and non-candidates ($< 5\sigma'$) with large uncertainties. The inset plot shows the histogram of excess significances (σ') as defined in A12.

distinct populations become apparent at $W1-W3 \approx 1.5$ and $W2-W3 \approx 1$, as is shown in Figure 3. Using these criteria as *WISE* color cuts, we kept only stars that fell below the two previously stated colors for computing $r-z$ polynomials, giving us 2,209 and 2,042 stars for each cut, respectively. A12 used a sigma-clipping method to derive their fourth order polynomials of the form,

$$color(p) = a_0 + a_1 p + a_2 p^2 + a_3 p^3 + a_4 p^4,$$

where p is the effective temperature proxy used, in our case $r-z$ color. We chose to implement a Bayesian framework to compute our fourth order polynomial. To estimate each coefficient for our polynomial we used `emcee`[8] (Foreman-Mackey et al. 2013), a Python implementation of the affine-invariant Markov Chain Monte Carlo (MCMC) ensemble sampler (Goodman & Weare 2010). Our coefficients, taken as the 5$^{\rm th}$ percentile values from `emcee`, are listed in Table 1 and the polynomials are shown in SDSS and *WISE* color-color space in Figure 3. Using the same definition for σ', we recomputed values for our sample and kept only stars with $\sigma' \geq 5$. After these cuts we were left with 300 stars showing excess flux at 12 μm.

Any color selection criterion omitting $W4$ has the possibility of excluding stars with cold dust populations that peak at wavelengths longer than 12 μm. Therefore, we examined all stars with a SNR$_{W4} \geq 3$ prior to exclusion. We did not have enough stars with high S/N $W4$ measurements to recompute polynomials using $r-z$ color for excess $W4$ detections. Instead, we used the A12 polynomials for $W1-W4$ and $W3-W4$ and found that all 13 stars with a SNR$_{W4} \geq 3$ exhibited levels of MIR flux far greater than estimated photospheric levels ($\gg 5\sigma'$). Every star that showed an excess at 22 μm also showed an excess at 12 μm.

As a final quality check we inspected each candidate within the *WISE* image archives. For each candidate, we assigned a quality flag, defined in Table 2, with QUALITY = 1 representing the highest quality candidates and QUALITY = 4 representing the lowest quality candidates. These quality flags are available in the online catalog under the heading 'QUALITY'. We will refer to this sample of 175 disk candidates as the "combined sample" throughout this study.

Figure 4 shows the *WISE* color-magnitude diagram for our candidates stars showing IR excesses, and also nearby K- and M-type dwarfs (Reid & Gizis 1997; Reid et al. 2004, 2007), a statistically older population of stars without known disks. The A12 polynomial describing the main sequence is over plotted (blue solid line). The population of nearby stars distinctly follows the A12 polynomials.

If we assume that for a given $r-z$ color the spread of intrinsic $W1-W3$ color for the non-IR excess stellar population follows a symmetric distribution, then it is possible that some of our candidates are false-positives within the red tail of the distribution. Assuming that *WISE* should have been able to achieve 5σ sensitivity in $W3$ for any star with $J \leq 17$ ($\sim$0.177 mJy) in the W11 catalog (57,339 stars), then we expect less than one false positive at $\sigma' = 5$. Most of the stars in both our samples are well above the $5\sigma'$ level, therefore we expect all of our candidates to exhibit real excesses not attributable to intrinsic photospheric levels. We list the excess signif-

[8] http://dan.iel.fm/emcee

Table 1
$r-z$ Polynomial Coefficents

Color	a_0	a_1	a_2	a_3	a_4	χ^2
$W1-W3$	$0.0872^{+0.2238}_{-0.2127}$	$0.5527^{+0.3883}_{-0.4223}$	$-0.2869^{+0.2259}_{-0.1635}$	$0.06287^{+0.06699}_{-0.07006}$	$-0.004410^{+0.006476}_{-0.006269}$	1.3118
$W2-W3$	$0.3776^{+0.2069}_{-0.1972}$	$-0.04019^{+0.37338}_{-0.38995}$	$-0.0054^{+0.2829}_{-0.2112}$	$0.002268^{+0.065797}_{-0.068222}$	$0.000299^{+0.006427}_{-0.006227}$	1.0543

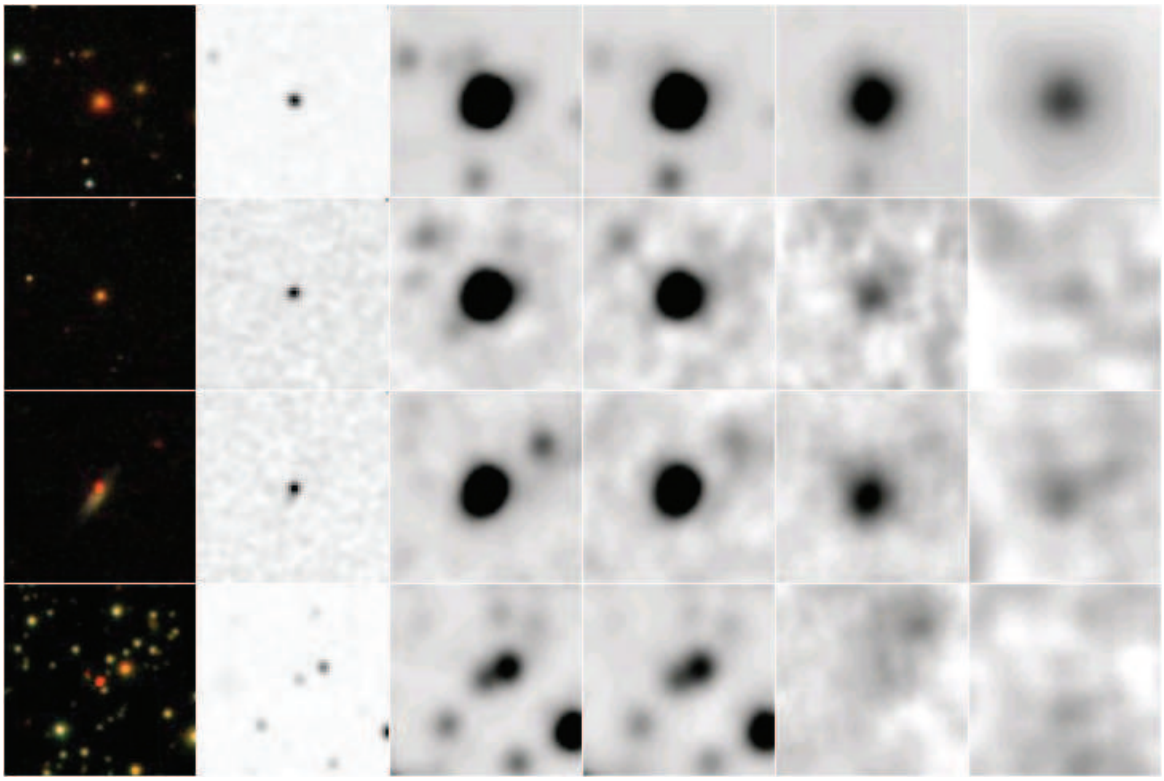

Figure 2. Images in SDSS (*gri* composite), 2MASS J, and *WISE* (3.4, 4.6, 12, and 22 μm, respectively) centered on the 3.4 μm source; each image is $1' \times 1'$. Top row: Example of an object that was included in our combined sample with QUALITY = 1. Second row: Example of an object that was included in our combined sample with QUALITY = 2. Third row: Example of a star that was not included in our sample due to superposition of a galaxy in SDSS. Bottom row: Example of a star that was not included in our sample due to crowding.

Table 2
WISE Quality Flags

Flag	Description	Number
1	Clear 12 and 22 μm source.	5
2	Clear 12 μm source with a 22 μm source that may be: affected by contamination, slightly offset, or low S/N.	11
3	Clear 12 μm source with no obvious 22 μm source.	54
4	12 μm source that may be: affected by contamination, slightly offset, or low S/N.	105

icances (σ') in Table 3 and in the online catalog.

Coordinates, distances, and spectral types are listed in Table 3. One of our stars was re-spectral typed from an M9 to an L0 in Schmidt et al. (2010), however, we chose not to remove this star from our sample. The distributions of spectral types, distances, and height above the Galactic plane are shown in Figure 5. Galactic heights were estimated following Bochanski et al. (2010) with $R_\odot = 8.5$ kpc (Kerr & Lynden-Bell 1986) and $Z_\odot = 15$ pc above the Galactic plane (Cohen 1995; Ng et al. 1997; Binney et al. 1997). The majority of stars in our samples are found within 500 pc from the Galactic plane. In Figure 6 we show the locations and distances of the sample plotted over a dust map, created using data from the *Cosmic Microwave Background Explorer* (*COBE;* Boggess et al. 1992, and references therein) and *IRAS* (Schlegel et al. 1998). We have seven candidate stars within the footprint of the Orion OB1 association (Warren & Hesser 1977). Although there appears to be structure in Figure 6, this is due to the SDSS sky coverage which is observed in wide 2.5° stripes, and all our candidates are spread throughout the SDSS DR7 footprint[9].

To test for additional spatial structure among our candidates, we wrote a simple friends-of-friends algorithm

[9] http://www.sdss.org/dr7/coverage/

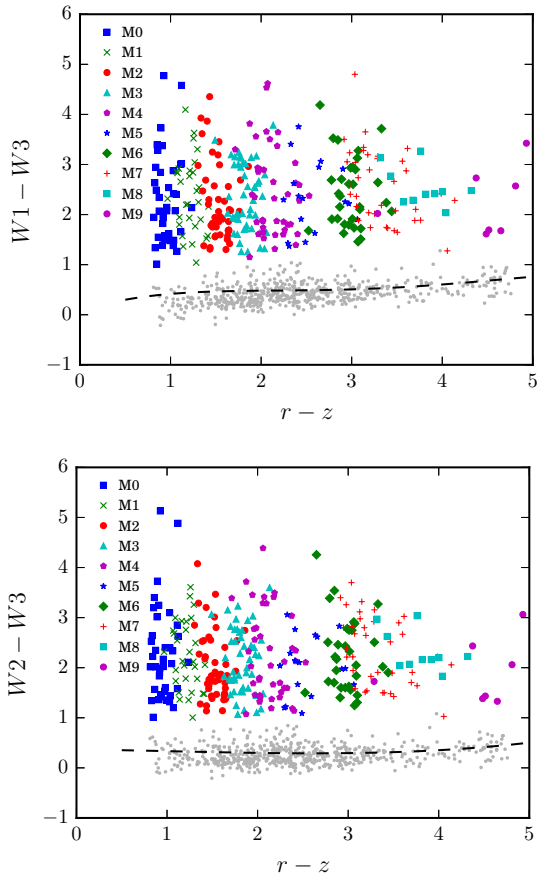

Figure 3. Color-color diagrams for the 309 stars showing 12 μm excesses as defined by A12. Stars are separated by spectral type using the colors and symbols in the legend. Non-excess stars ($< 5\sigma'$; 2,185 stars) are plotted as grey points. The dashed lines represent our computed polynomials used to trace the main sequence M dwarfs.

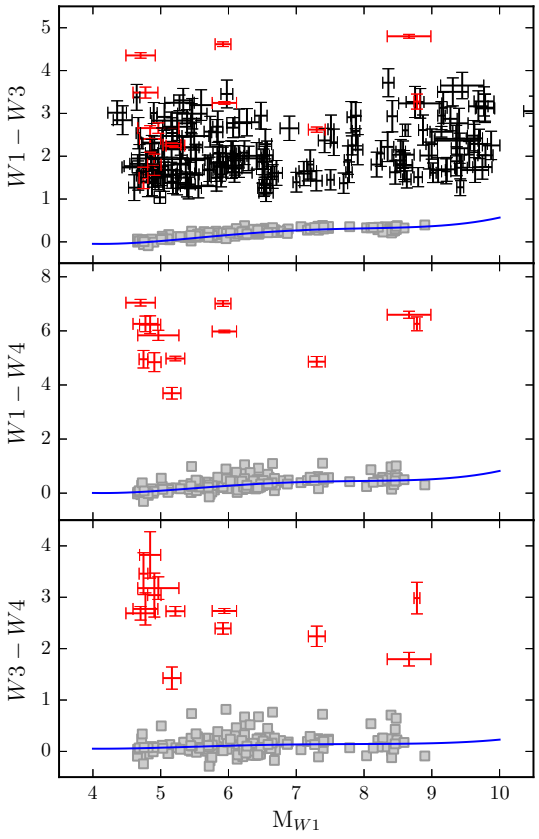

Figure 4. *WISE* color-magnitude diagrams. Disk candidates from this study (pluses) and the nearby K and M dwarfs (squares; Reid & Gizis 1997; Reid et al. 2004, 2007) are shown. Only stars with $\mathrm{SNR}_{W4} \geq 3$ and $\mathrm{CC_FLAGS}_{W4} = 0$ were used in the $W1-W4$ and $W3-W4$ plots (red pluses). Overplotted are the main sequence color polynomials from A12 (solid lines). Both populations are well separated indicating that the vast majority of these stars likely harbor dust populations. Even if distance errors were as large as 50%, which would move the points to the left/right on each plot, the excesses we observe would still be statistically significant.

(FoF; Huchra & Geller 1982). We used the most general method for finding groups and used a distance discriminator to determine if two stars were "friends," arbitrarily choosing a critical length scale of 10 pc. The size is somewhat arbitrary depending on whether members make up: 1) a cluster, in which case members will be closely grouped in position; or 2) a moving group, in which case members will be closely grouped in velocity space. We only tested for spatial structure corresponding to the distribution of candidates throughout the Galaxy. Using 3-dimensional position vectors, made by combining photometric parallax distances and the positions of our stars, we were able to group stars together by their positions within the Galaxy. With our method we found two stellar groupings (available in the online catalog), one of which was centered on Orion. Neither of these stellar groupings appeared to have significantly similar kinematics (kinematics computed in §4.3), and are likely not members of a moving group.

2.2. *Interstellar Reddening*

The interstellar medium (ISM) contains varying amounts of dust, which affect observations depending on their line-of-sight (LOS) by absorbing or scattering background light. These effects "redden" or "extinct" observed fluxes, and are most significant at short wavelengths, falling off in the MIR (e.g., Fitzpatrick 1999). For stars within ∼50 pc, extinction effects can typically be ignored due to the lack of dust within the local bubble (Lallement et al. 2003). Due to the distances to the stars in this study, effects from interstellar extinction may be significant and should be accounted for.

To correct for the effects of dust, Schlegel et al. (1998) created dust maps by measuring galactic extinction using *COBE* and *IRAS*. Although SDSS provides extinction estimates for photometric sources using these maps, caution must be taken due to the fact that the Schlegel et al. (1998) dust maps estimate the *total* extinction along a LOS out of the Galaxy. SDSS stars at distances of hundreds of parsecs might have their fluxes reduced by only a fraction of the total extinction measured in these maps, requiring us to estimate extinction not only along a LOS, but as a function of distance. Extinction effects due to circumstellar dust are also possible if these are pre-main sequence stars. However, extinction due to circumstellar dust will only have a significant effect if the star is a protostar (< 1 Myr) and still harbors an infalling envelope, or the disk is seen edge-on (for a more detailed explanation see Hartmann 1998). Measured extinction effects cannot be reliably attributed to interstellar mate-

Table 3
Disk Candidate Parameters

Catalog Number	R.A. (J2000.0) (deg)	Decl. (J2000.0) (deg)	SpT[a] ±1	d[b] (pc)	Z (pc)	A_V[c] (mags)	R_V[d]	σ'_{W1-W3}[e]	σ'_{W1-W4}[e]	σ'_{W3-W4}[e]
40.....	83.032543	0.284724	M2	195	-44	0.52 ± 0.02	3.1	63.7	21.4	8.8
42.....	83.296678	0.232939	M3	128	-23	0.35 ± 0.06	3.1	111.6	153.4	76.3
62.....	129.436350	21.646841	M7	108	73	0.00 ± 0.00	3.1	119.0	60.5	17.5
78.....	142.779528	10.102017	M6	135	101	0.77 ± 0.06	3.1	20.0	29.0	13.0
108.....	180.890419	49.244348	M1	648	607	0.00 ± 0.03	3.1	8.7	17.5	9.8
110.....	181.192639	40.432928	M4	475	471	0.16 ± 0.05	3.1	97.3	83.7	29.0
115.....	185.176759	48.151921	M0	894	844	0.15 ± 0.03	3.1	9.3	24.0	11.7
126.....	203.510751	10.271275	M2	872	836	0.13 ± 0.01	3.1	81.4	73.6	27.9
140.....	232.129207	38.051640	M5	150	138	0.15 ± 0.11	3.1	45.9	29.8	14.9
142.....	232.736020	20.902880	M1	657	540	0.00 ± 0.00	3.1	26.0	39.5	19.9
152.....	236.977925	52.815983	M1	283	227	0.00 ± 0.03	3.1	56.2	73.2	40.6
156.....	238.196155	35.302076	M3	1174	923	0.35 ± 0.04	3.1	32.7	27.6	12.2
164.....	284.933373	78.072385	M0	723	332	0.00 ± 0.00	3.1	7.2	19.4	11.7

Note. — Values listed only for stars with $\mathrm{SNR}_{W4} \geq 3$. Values for the entire sample from this study are available online.
[a] Determined in West et al. (2011).
[b] Photometric distances have typical uncertainties of ∼20% (Bochanski et al. 2010; Jones et al. 2011).
[c] Measured in Jones et al. (2011).
[d] Adopted parameters from Jones et al. (2011) measurements.
[e] σ' values from A12. These represent the IR excess significance in two *WISE* bands.

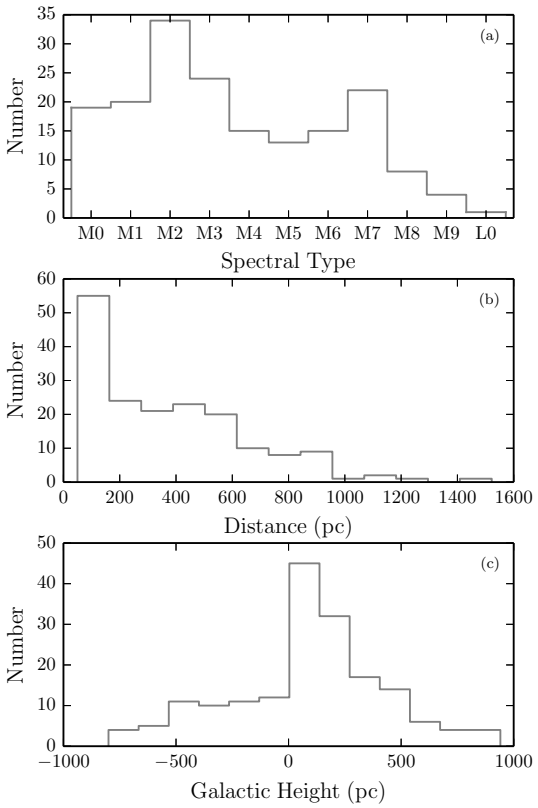

Figure 5. Distributions of the combined sample: (a) spectral type distribution; (b) distance distribution; (c) distribution of vertical distance away from the Galactic plane. The majority of stars are earlier spectral types (< dM5) within $d < 600$ pc and $|Z| < 500$ pc.

rial or a circumstellar disk, since the effect is cumulative for all sources of extinction. For the purposes of this paper, we assume the disk material to be optically thin at all observed wavelengths since none of our stars are protostars.

Jones et al. (2011, hereafter J11) measured the total interstellar extinction, A_V, and the ratio of total extinction to reddening, R_V, for the W11 catalog. This was done by comparing the spectra for each star in the W11 catalog to high S/N SDSS spectra for nearby M dwarfs at low or zero extinction lines-of-sight. Using the A_V and R_V values from J11, along with relative extinction A_λ/A_V, the ratio of extinction in a given bandpass to extinction in the V-band, measurements from the Asiago Database (Moro & Munari 2000; Fiorucci & Munari 2003), we calculated the extinction for each SDSS, 2MASS, and *WISE* photometric band. V-band extinction is commonly used for relative extinction values in the optical due to extinction laws being expressed in terms of A_V and R_V. The Asiago Database contains measured relative extinction values for the SDSS and 2MASS photometric systems (e.g., A_r/A_V, A_{K_s}/A_V, etc.) using the Fitzpatrick (1999) extinction law. To estimate relative extinction values for the SDSS and 2MASS photometric systems, bandpass response curves were convolved over a model M-spectral type photosphere to determine the relative extinction for each bandpass (for more details see Moro & Munari 2000; Fiorucci & Munari 2003). These relative extinction measurements for the SDSS and 2MASS bandpasses allowed us to estimate specific bandpass extinctions using the A_V values from J11 (e.g., $A_r = (A_r/A_V)A_{V_{J11}}$).

For $W1$ and $W2$, we used relative extinction A_λ/A_K measurements for *Spitzer*'s Infrared Array Camera (IRAC; Fazio et al. 2004) channel 1 (3.6 μm) and channel 2 (4.5 μm) from Indebetouw et al. (2005), which are analogous to $W1$ and $W2$ (D. P. Clemens, personal communication). For wavelengths longer than 5 μm the extinction curve begins to flatten, and we assumed equal extinction values for $W2$, $W3$, and $W4$. The extinction parameters used for this study are listed in Table 4. Extinction corrected photometry is included in the online catalog. The majority of our sample (∼90%) had relatively small amounts of extinction ($A_V \leq 0.5$), with V-band extinction values as high as 3.1 mags. Our typical extinction values are smaller than those measured around

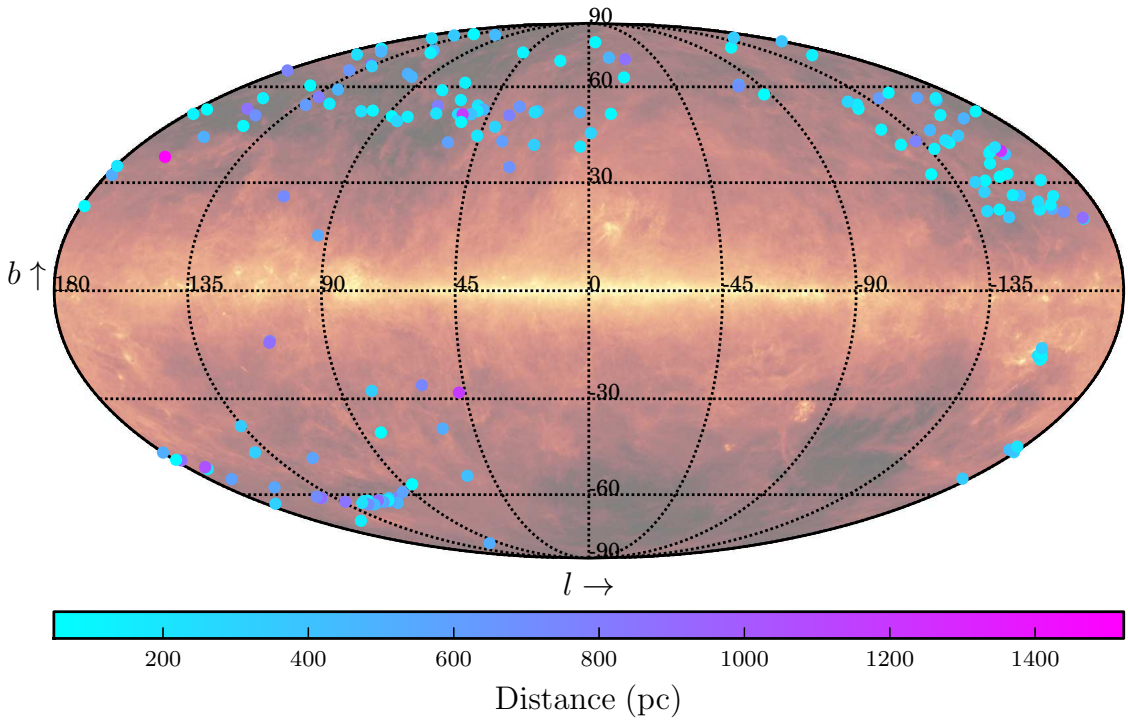

Figure 6. Galactic coordinates and distances of disk candidates from this study. Stars are color-coded by distance. The points are plotted on the *IRAS/COBE* 100 μm dust map (Schlegel et al. 1998). 94% of the sample is located off the Galactic plane ($|b| > 20°$). seven of the 11 stars with $|b| \leq 20°$ are found within nearby proximity of the star-forming Orion OB1 association ($l \approx -156°$, $b \approx -16°$, $d \approx$ 200–500 pc; Bally 2008).

nearby star-forming regions (A_V = 1–12; Luhman et al. 2003; Luhman 2004; McClure 2009), as expected for field stars.

2.3. *Flux Conversions from Magnitudes*

Flux densities for SDSS asinh AB magnitudes were computed following the methods outlined in the DR7 flux calibration primer[10]. 2MASS Vega magnitudes were converted to flux densities following the steps outlined in the explanatory documentation[11]. *WISE* Vega magnitudes were converted to flux densities following the all-sky explanatory supplement[12], assuming a spectral slope of -2 ($F_\nu \sim \nu^{-2}$). For extremely red sources (e.g., ultra-luminous infrared galaxies), it was found that $W4$ overestimated fluxes by $\sim$10% since the stellar sources used to photometrically calibrate *WISE* were significantly bluer in comparison (e.g., A-K dwarfs and K/M giants). Since we expect warm dust to mimic an extremely red source, we applied flux corrections to $W4$, reducing measured fluxes by 10%. It is also expected that red sources should have their $W3$ fluxes underestimated by $\sim$10%, however, we chose not to apply this correction since the shape of the SED at $W3$ is not known a priori.

3. EVALUATING THE DISK CANDIDATES

To properly characterize the dust content for each star, we first estimated the expected flux of the star using model stellar photospheres. We used a pre-computed grid of BT-Settl models (Allard et al. 2012b,a), computed with the PHEONIX atmosphere code (Hauschildt et al. 1999; Allard et al. 2001), to determine stellar photospheric flux with which to fit optical and NIR photometry. For each star, we used grids spanning $T_{\rm eff}$ between $\pm$1,000 K of nominal values, determined by using spectral types from W11 and $T_{\rm eff}$ values from Reid & Hawley (2005), in increments of 100 K. The other parameters spanned by the grids were $\log(g)$ in the range [0.5, 6.0] in increments of 0.5 dex, and metallicity [M/H] in the range [$-$2.5, 0.5] in increments of 0.5 dex. All of the observed photometry was color-corrected for extinction effects (§2.2).

To fit the stellar photosphere models to our photometry, we computed a χ^2 minimization as a function of the effective temperature, surface gravity, and metallicity. We performed two separate fits, one to the photometry and one to the SDSS spectrum. We gave equal weights to both the photometric and spectral fits because we found that separate fits typically agreed to within $\pm$100 K. The SDSS spectra were radial velocity and extinction corrected using J11 extinction values (§2.2) and the extinction law from Fitzpatrick (1999) prior to fitting. The spectrum and model photosphere were normalized to their values at 7500 Å. The model photosphere was then resampled to SDSS wavelengths while conserving flux using the Python package *Pysynphot*[13].

For the photometric fit, the modeled photospheric flux was integrated over the *ugriz* and *JHK*$_s$ relative spectral response curves (RSRs) to produce synthetic magnitudes, which we matched to our observed photometry for the χ^2 minimization. *WISE* bands were omitted due to

[10] http://www.sdss.org/dr7/algorithms/fluxcal.html
[11] http://www.ipac.caltech.edu/2mass/releases/second/doc/sec6_4a.html
[12] http://wise2.ipac.caltech.edu/docs/release/allsky/expsup/sec4_4h.html
[13] http://stsdas.stsci.edu/pysynphot/

Table 4
Adopted Reddening Parameters

R_V[a]	A_u/A_V[b]	A_g/A_V[b]	A_r/A_V[b]	A_i/A_V[b]	A_z/A_V[b]	A_J/A_V[b]	A_H/A_V[b]	A_K/A_V[b]	A_{W1}/A_K[c]	A_{W2}/A_K[c]
2.1	2.06	1.28	0.78	0.56	0.43	0.27	0.18	0.12	0.56	0.43
3.1	1.67	1.19	0.84	0.62	0.46	0.27	0.17	0.12	0.56	0.43
5.0	1.38	1.12	0.88	0.67	0.49	0.26	0.16	0.11	0.56	0.43

[a] Adopted R_V was based on measurements from J11: $R_V = 2.1$ for $0 < R_{V_{J11}} < 2.5$; $R_V = 3.1$ for $2.5 \leq R_{V_{J11}} < 4$; $R_V = 5$ for $4 \leq R_{V_{J11}} < 10$.
[b] Adopted from Moro & Munari (2000); Fiorucci & Munari (2003) (see text).
[c] Adopted from Indebetouw et al. (2005) (see text).

expected deviations from the stellar photosphere in $W3$ and $W4$ and possible deviations in $W1$ and $W2$ for pre-transitional disk structures (Espaillat et al. 2007, 2011). The 2MASS RSRs were taken from Cohen et al. (2003), *WISE* RSRs from Wright et al. (2010), and SDSS RSRs from Doi et al. (2010). All RSRs were normalized to unity at the peak value of each band. Each photometric band was weighted by the inverse variance of the photometric values. Synthetic measurements were normalized to the observed K_s magnitude for fitting. The results of our fitting method can be seen in Figure 7. The average errors in our fits were $\sigma_{T_{\rm eff}} < 200$ K, $\sigma_{\rm [M/H]} < 1$, and $\sigma_{\log(g)} < 1$.

The primary purpose of our stellar model fits was to estimate the stellar SEDs and ascertain the amount of excess IR flux, and not to derive robust fundamental stellar parameters. The shape of the SED is dependent primarily on the stellar effective temperature ($T_{\rm eff}$), and less so on the metallicity or surface gravity. Allowing all three parameters to float gave us better estimates on $T_{\rm eff}$ and the uncertainty in our fit. The best-fit $T_{\rm eff}$ for our candidates are listed in Table 5, and we include all model parameters and chi-squared values in the online catalog. There is one clear outlier in the M4 spectral type bin, possibly due to enlarged photospheres owing to a young age. This star will be discussed further in §4.6.1.

For completeness, we also include the traditional χ metric for measuring excesses in the IR defined as,

$$\chi_\lambda = \frac{F_\lambda - F_{*,\lambda}}{\sigma_\lambda}, \quad (1)$$

where F_λ is the observed flux at wavelength λ, $F_{*,\lambda}$ is the expected stellar flux at wavelength λ, and σ_λ is the uncertainty in the measurement at wavelength λ. This method depends only on estimating $T_{\rm eff}$, which our above process was able to do within a few hundred kelvin for most of our stars (e.g., see Figure 13). Within our combined sample, all stars were found to have $\chi_{12} > 2$, and every star with a $\rm SNR_{W4} \geq 3$ had $\chi_{22} > 3$. We chose not to remove any candidates with $\chi_{12} \leq 3$ from our sample as these stars all had higher significances using the method of A12 (§2.1.1), which is a purely empirical method that does not depend on stellar models. These values are included in the online catalog, along with flux densities for *WISE* observations and expected stellar photospheric levels.

3.1. *Binarity*

We investigated the possibility that the IR excesses in our stars are due to ultracool companions. To estimate the expected observational signature of ultracool companions, we created combined SEDs for low-mass binaries. To properly scale the photospheric flux density for the M dwarf and the ultracool companion, we used the luminosity-$T_{\rm eff}$ relations from Reid & Hawley (2005) for M dwarfs, and the maximum values from Baraffe et al. (2003) for ultracool companions. To scale the model flux density to an observed flux density, we integrated the flux density for each model (star and companion), and scaled the flux density to the expected luminosity from the lit-

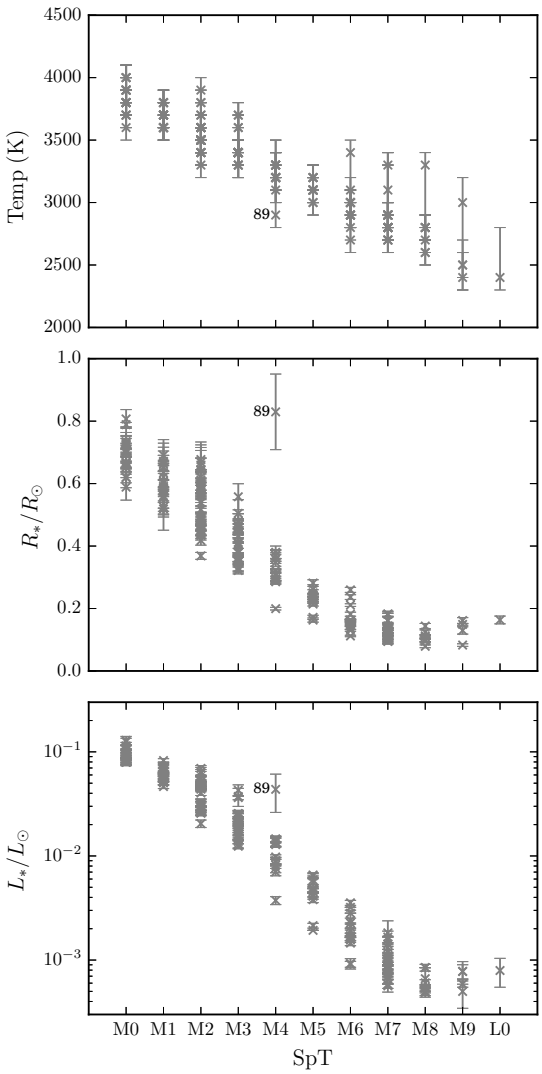

Figure 7. Best fit parameters from our SED fitting method as a function of spectral type for our combined sample. The majority of stars appear to follow the expected trends for temperature, luminosity, and radius. The outlier in the M4 spectral type (marked by its candidate number) will be discussed in §4.6.1.

Table 5
Model Parameters

Catalog Number	T_* [a] (K)	L_* ($10^{-2}L_\odot$)	R_* ($R_\odot$)	$T_{\rm dust}$ (K)	$L_{\rm dust}/L_*$ [b]	$D_{\rm min}$ [b] (AU)	$M_{\rm dust}$ [b] ($M_{\rm Moon}$)	$\chi^2_{\rm fits}$ [c]
40.....	3600^{+100}_{-100}	6.24 ± 0.52	0.64 ± 0.04	325^{+15}_{-15}	3.5×10^{-2}	0.18	2.0×10^{-5}	33.85
42.....	3400^{+200}_{-100}	1.75 ± 0.15	0.38 ± 0.03	185^{+10}_{-10}	$> 2.7 \times 10^{-1}$	0.30	4.0×10^{-4}	321.87
62.....	2800^{+600}_{-100}	0.10 ± 0.03	0.14 ± 0.02	290^{+10}_{-5}	$> 5.9 \times 10^{-1}$	0.03	8.5×10^{-6}	28.39
78.....	3000^{+100}_{-100}	0.19 ± 0.01	0.16 ± 0.00	165^{+20}_{-20}	2.3×10^{-1}	0.12	6.0×10^{-5}	17.53
108.....	3600^{+100}_{-100}	6.58 ± 0.32	0.66 ± 0.03	155^{+25}_{-35}	6.3×10^{-2}	0.83	7.2×10^{-4}	22.26
110.....	3200^{+200}_{-100}	1.36 ± 0.13	0.38 ± 0.02	220^{+5}_{-10}	~ 1	0.19	5.8×10^{-4}	15.48
115.....	3900^{+100}_{-100}	9.20 ± 0.38	0.67 ± 0.05	125^{+20}_{-25}	2.0×10^{-1}	1.51	7.5×10^{-3}	24.99
126.....	3600^{+100}_{-100}	4.03 ± 0.22	0.52 ± 0.05	195^{+5}_{-10}	$> 9.8 \times 10^{-1}$	0.41	2.7×10^{-3}	37.82
140.....	3200^{+100}_{-100}	0.64 ± 0.03	0.26 ± 0.01	220^{+10}_{-10}	8.2×10^{-2}	0.13	2.2×10^{-5}	42.21
142.....	3700^{+100}_{-100}	5.73 ± 0.51	0.58 ± 0.08	155^{+10}_{-10}	1.7×10^{-1}	0.77	1.7×10^{-3}	23.98
152.....	3600^{+100}_{-100}	5.45 ± 0.30	0.60 ± 0.04	175^{+10}_{-10}	6.4×10^{-2}	0.59	3.7×10^{-4}	10.50
156.....	3700^{+100}_{-100}	3.63 ± 0.17	0.47 ± 0.04	185^{+15}_{-15}	$> 4.9 \times 10^{-1}$	0.43	1.5×10^{-3}	15.56
164.....	3800^{+100}_{-100}	8.37 ± 0.43	0.67 ± 0.02	130^{+20}_{-30}	7.1×10^{-2}	1.33	2.1×10^{-3}	11.21

Note. — Values listed only for stars with $\rm SNR_{W4} \geq 3$. Values for the combined sample are available online.
[a] Upper and lower limits derived from the 1σ spread in reduced χ^2 values.
[b] Typical uncertainties are on the order of $\sim$20%
[c] To estimate the uncertainty in our fits we used a $\chi^2 - \chi^2_{\rm min}$ procedure similar to Mohanty et al. (2010).

erature at an arbitrary distance. The distance falls out of the equation due to the fact that we compute ratios of fluxes densities over integrated bandpasses. Mathematically, this is shown as:

$$F_{\lambda,\rm scaled} = \frac{CL_\odot}{4\pi d^2 \int_0^\infty B_\lambda \, {\rm d}\lambda} \times F_{\lambda,\rm model}, \qquad (2)$$

where C is the constant used to scale the luminosity with effective temperature (or spectral type) taken from Reid & Hawley (2005) and Burrows et al. (1997), d is an arbitrary distance, B_λ is the blackbody flux density at the effective temperature of the star or ultracool companion, and $F_{\lambda,\rm model}$ is the model flux density.

We used solar metallicity for both the M dwarf and ultracool companion, $\log(g) = 5$ for the ultracool companion, and $\log(g) = 3$ & 5 for the M dwarf to produce a range of values. After scaling each photospheric flux density, we co-added the models and performed synthetic photometry on the combined model to produce flux ratios using the zK_sW1-bands relative to the $W3$-band. We then used these synthetic flux density ratios to compare against our observed flux density ratios and determine if any of our excesses could be explained by an ultracool companion. Our model values are shown in Figure 8. Although two of our candidates fell within the range of harboring an ultracool companion in the F_z/F_{W3} ratio, they did not meet the threshold in other flux ratios, indicating that their excesses are likely not originating from a companion. Focusing on the F_{W1}/F_{W3} ratios, we find that all of our sources have IR excesses much larger than those attributable to an ultracool companion by $\gg 3\sigma$. To test the sensitivity of our model, we applied our method to a known dM+ultracool binary (M9/T5) from Burgasser et al. (2012), and found that our method effectively detected this low-mass binary within the uncertainties (also shown in Figure 8).

3.2. *Galactic and Extragalactic Contamination*

Recent studies of cold disk populations ($T \approx 22$ K) using *Herschel* have investigated the possibility that detections of IR excess may be due to IR cirrus/Galactic background or extragalactic contamination (e.g., Eiroa et al. 2011; Krivov et al. 2013; Gáspár & Rieke 2014). To ensure our excesses are not simply chance alignments of background objects, we must consider and account for both Galactic and extragalactic sources of contamination.

3.2.1. *Galactic Background Contamination*

Kennedy & Wyatt (2012, hereafter KW12) investigated *WISE* excesses for stars in the *Kepler* field-of-view (FOV). Due to the close proximity of the *Kepler* FOV to the Galactic plane, KW12 found a considerable gradient in the number of stars exhibiting $W3$ excesses as a function of distance from the plane, with larger excess source counts closer to the Galactic plane. They attributed this gradient to higher levels of background contamination closer to the Galactic plane, where the ISM has a higher density. Using the Improved Processing of the *IRAS* Survey (IRIS; Miville-Deschênes & Lagache 2005) 100 μm maps[14], KW12 determined empirically that stars within a 100 μm background level greater than 5 MJy steradian^{-1} were prone to Galactic contamination. A major concern of KW12 was that the *WISE* estimated background level (W3SKY) was smooth and did not trace the clumping of the $W3$ excesses seen within the *Kepler* FOV. KW12 used the *WISE* all-sky source catalog, which has been found to *underestimate* the background level in $W2$, $W3$, and $W4$[15], and hence *overestimate* the

[14] http://www.cita.utoronto.ca/ mamd/IRIS/
[15] http://wise2.ipac.caltech.edu/docs/release/allwise/expsup/sec2_3a.html

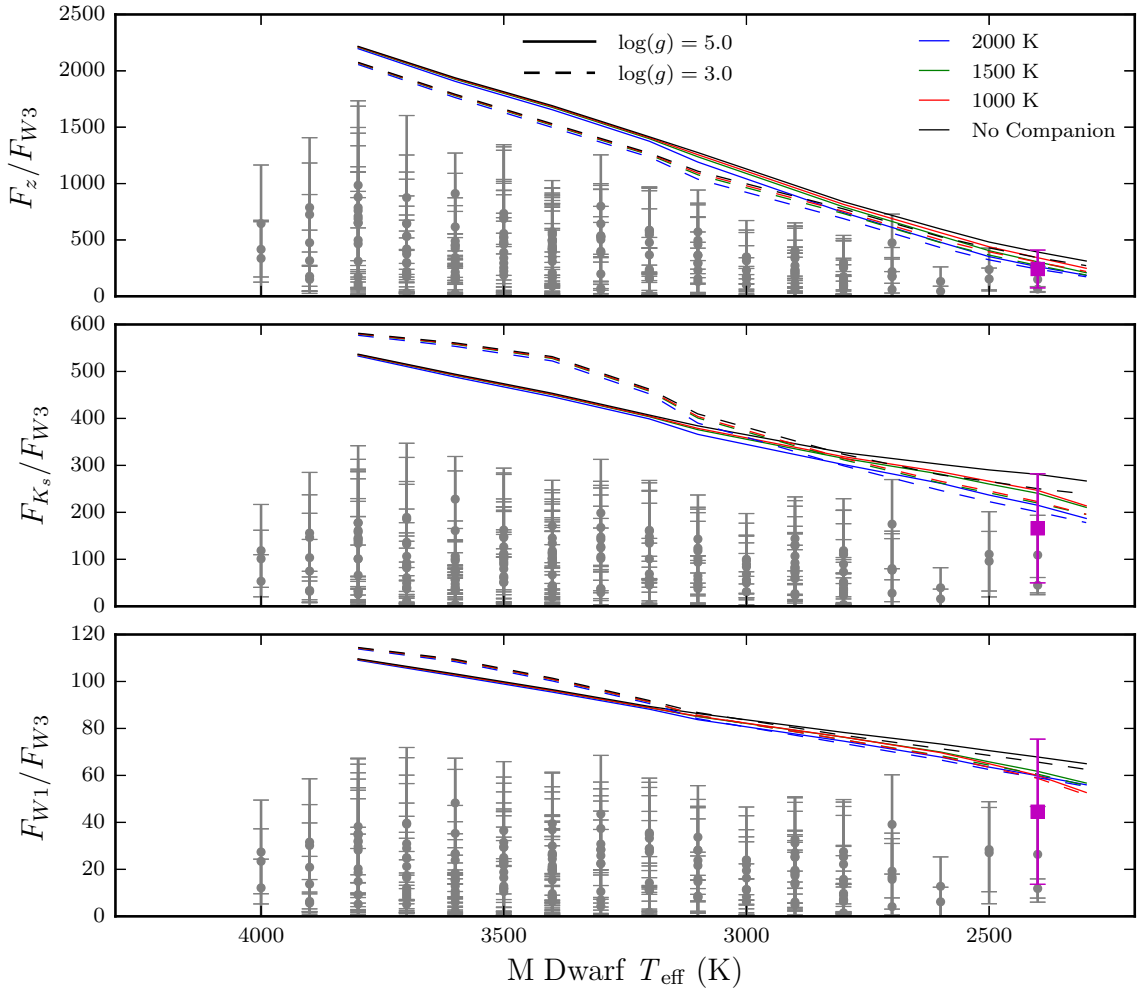

Figure 8. Flux density ratios for dM+ultracool companion binary cases. Flux density ratios are taken from SEDs modeled as coadded SEDs of an M dwarf and an ultracool companion. This combined SED represents what is expected from a spectroscopic binary made-up of an M dwarf and an ultracool companion. Each line represents a model of the flux density ratio between two bands for an M dwarf with an ultracool companion (colored lines) and a single M dwarf with no companion (black lines). M dwarf temperatures are listed on the x-axis and companion temperatures are listed in the top right. For the M dwarf, we considered two separate surface gravities, represented by the solid ($\log(g) = 5$) and dashed lines ($\log(g) = 3$). Stars from our combined sample are plotted (gray circles), with error bars representing the 3σ limits. Stars that fall below the model lines have more 12 μm flux than the binary case, and thus an IR excesses larger than can be attributed to an ultracool companion. In the W1/W3 flux ratio, all of the stars exceed the IR excess flux attributable to an ultracool companion at $> 3\sigma$ confidence. Also plotted is the low-mass binary (M9/T5; magenta square) from Burgasser et al. (2012). Our model is able to reproduce this binary within its 3σ uncertainty.

measured flux in these bands for the source[16]. The AllWISE source catalog used for our study employs a new method to estimate background noise levels, reducing the number of overestimated flux measurements in $W2$, $W3$, and $W4$.

The majority of W11 stars were sampled at high Galactic latitudes, however, there were a few areas sampled close to the Galactic plane. To test for contamination we used the IRIS 100 μm maps to determine the background levels for our stars. We found that the majority of stars fell below the KW12 cut of 5 MJy steradian^{-1}, as shown in Figure 9. Most of the candidates with a background level higher than 5 MJy steradian^{-1} were found in Orion, which we expect to have a high background. Overall, we do not find an overabundance of sources within areas of high background flux, as seen by KW12. This indicates that the AllWISE source catalog has a robust method for determining background noise levels, significantly reducing the number of false positive excess sources within the catalog. We conclude that our observed excesses do not originate from Galactic background contamination, and did not to remove any candidates falling within regions of high 100 μm IRIS fluxes.

3.2.2. *Extragalactic Contamination*

Due to the large FWHM of the *WISE* 12 μm (6.5″) and 22 μm (12″) PSFs, contamination through chance alignment with an extragalactic source is a serious concern and must be addressed. A chance alignment with an object that is bright in the IR, but obscured in the optical (e.g., ultra-luminous infrared galaxies) could contribute large amounts of IR flux. We used two different methods to test the likelihood of such a chance alignment. The *WISE* photometric pipeline departs from classical

[16] http://wise2.ipac.caltech.edu/docs/release/allwise/expsup/sec5_3biii.html

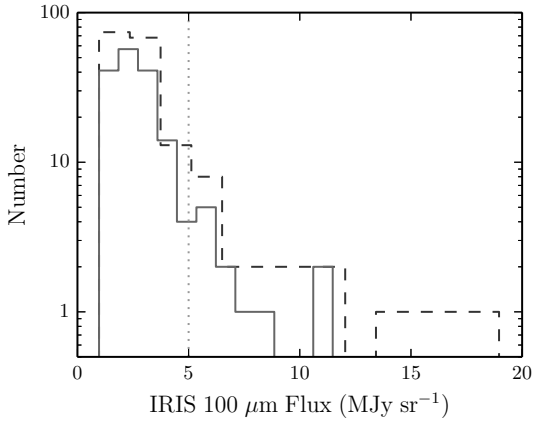

Figure 9. Source counts as a function of IRIS 100 μm flux level. Shown are our combined sample (dashed line), and our combined sample without the Orion candidates (solid line). The majority of our sources fall below the 5 MJy steradian^{-1} cut used by KW12 (dotted line). The Orion candidates make up a significant fraction of the stars that fall above 5 MJy steradian^{-1}.

photometric methods by performing profile-fit photometry simultaneously across all bands[17]. This method is expected to detect fainter sources, and reduce confusion. However, without correlating extracted source positions between each band, there is a contamination risk from a background source that was faint at 3.4 and 4.6 μm, but relatively bright at 12 and/or 22 μm.

We chose to employ a more traditional source detection technique by acquiring *WISE* archive images and performing source extraction via SExtractor (Bertin & Arnouts 1996). For sources that are detectable in $W1$, $W2$, and $W3$ bands, we expect small offsets between their extracted positions within each separate band since they have similar PSF FWHMs (6.1″, 6.4″, and 6.5″, respectively), and the astrometric precision of *WISE* is typically $\lesssim 0.5''$[18]. We obtained $10' \times 10'$ images in 3.4, 4.6, and 12 μm from the *WISE* image archives[19]. We used a setup of SExtractor, optimized for *WISE* images[20], on each *WISE* band separately. We compared the positions of sources extracted using SExtractor in the 3.4, 4.6, and 12 μm bands, using the closest extracted source to our expected source position based on the astrometry within the calibrated *WISE* FITS header. We fit the core of the offset distributions (R.A. and Dec.) and found for the 3.4/4.6 μm offsets, each distribution had $\mu \approx 0$ and $\sigma \approx 1''$, and the 3.4/12 μm offsets had $\mu \approx 0$ and $\sigma \approx 5''$. Sources that had offsets $> 1''$ in the 3.4/4.6 μm comparison failed extraction at 4.6 μm; these sources were found to have nearby bright sources as well as faint source detections, likely confusing SExtractor. Examples of objects that failed detection at 4.6 μm are shown in Figure 10. Figure 11 shows the results comparing the 3.4/12 μm source positions.

To test if this scatter is intrinsically due to the precision of *WISE* astrometry or a sign of contamination, we compared it against a subsample of SDSS DR10 quasars (166,583 quasars; Pâris et al. 2014), extragalactic objects

[17] http://wise2.ipac.caltech.edu/docs/release/allsky/expsup/sec4_4c.html
[18] http://wise2.ipac.caltech.edu/docs/release/allwise/expsup/sec6_4.html
[19] http://irsa.ipac.caltech.edu/applications/wise/
[20] http://wise2.ipac.caltech.edu/staff/fmasci/SEx_WPhot.html

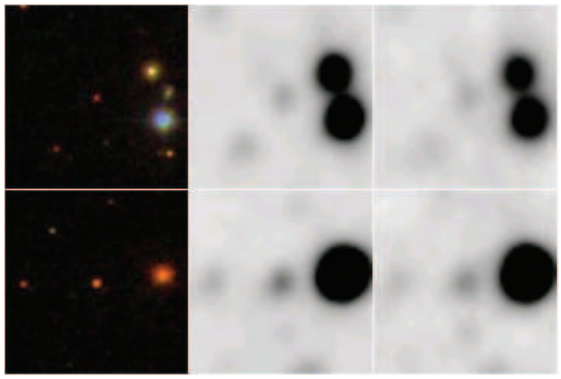

Figure 10. $1' \times 1'$ images in SDSS *gri* (left), $W1$ (middle), and $W2$ (right) for objects that failed SExtractor extraction at 4.6 μm. Nearby bright sources coupled with faint detections likely confuse SExtractor.

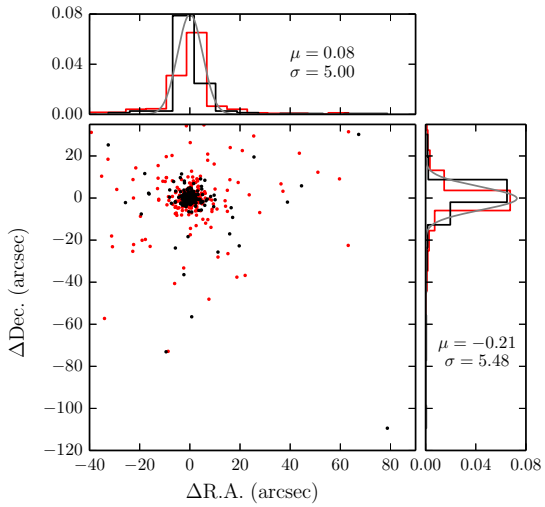

Figure 11. Difference in positions between sources extracted from the 3.4 and 12 μm bands for our sample (black) and the subsample of SDSS DR10 quasars (red). The best-fit normal distribution to our sample is plotted in gray (distribution parameters listed). For both distributions (stars and QSOs), there is a discrepancy between the 3.4 μm and 12 μm source positions for many of the sources extracted by SExtractor (see text).

that are bright and remain stationary on the sky. Following step #2 & #6 from §2.1, we used only quasars that did not have another SDSS DR10 object within 6″. We also chose only quasars at high Galactic latitudes ($b \geq 77°$) to reduce contamination from stellar sources. Lastly, we chose quasars with a similar $W3$ SNR distribution to our candidates, which were found primarily between $3 \leq \mathrm{SNR}_{W3} \leq 5$. Our final subset consisted of 304 quasars. We then followed the above procedure by obtaining $10' \times 10'$ images in 3.4, 4.6, and 12 μm from *WISE* and performed source extraction via SExtractor. As shown in Figure 11, we found a similar offset distributions for our subsample of quasars compared to our candidate disk stars (a K-S test gives p-value$_{\mathrm{R.A.}} = 0.25$ and p-value$_{\mathrm{Dec.}} = 0.16$). The long tails of the distributions to higher offsets ($\gtrsim 10''$) mark objects where SExtractor failed to extract a source near our source position, and instead selected the closest extractable source. We include extracted position offsets in the online catalog.

It is likely that SExtractor failed to extract our sources due to the low S/N threshold. We do not expect this to

be a limitation to the *WISE* pipeline, where the PSF is well characterized and the images are coadded, and the *WISE* passive deblending method should be more reliable than SExtractor deblending. Further investigation is required into the *WISE* pipeline to determine if source extraction from coadded images can be improved to include probabilities that each flux measurement is attributable to the same object in each band. The similarity of the quasar and disk candidate source position distributions likely implies a limitation to source extraction via SExtractor rather than a discrepancy in source position as all candidates were visually verified.

To further investigate the possibility of chance alignments, we estimated the extragalactic source density that might contaminate our fields. Recently, Yan et al. (2013) estimated the number of *WISE* extragalactic sources with $S/N_{W3} \geq 3$, at Galactic latitudes $|b| > 20°$, was 1,235 deg^{-2}. This background value was determined, down to a limiting flux density of ∼0.22 mJy ($W3 \approx 12.8$). Because the addition of the photospheric flux from a star plus the flux from chance alignment with an extragalactic source could create a high enough S/N flux to mimic an actual point-source detection, we expect our limiting flux density to be lower than the value found by Yan et al. (2013). Our sample includes objects with magnitudes up to $W3 = 12.727$ (∼0.236 mJy), however, we estimate that an extragalactic source that could potentially contaminate our sample could reach a magnitude of $W3 \approx 13$ (∼0.183 mJy), which is the approximate *WISE* detection limit for our sources (§4.5).

To estimate a new density of extragalactic sources down to $W3 = 13$, we sampled the AllWISE source catalog at 1,000 randomly chosen locations in the sky. We focused on Galactic latitudes $|b| \geq 60°$, since we expect fields at high Galactic latitudes to have the highest ratio of extragalactic to Galactic sources. We selected all sources (making no cuts on source morphology) within a 180″ radius of our randomly chosen sky position, and with $S/N_{W3} \geq 3$ and no contamination or confusion (CC_FLAGS = 0000). We repeated this process 15 times and found a source density of 976 ± 14 deg^{-2}, smaller than the value reported by Yan et al. (2013), likely due to our higher Galactic latitude cut. 976 sources is potentially higher than the number of actual extragalactic sources since there are also stars in these fields. Considering this, we chose to be conservative and used the value of 976 sources as the number of contaminants we might find within a solid angle of 1 deg^2 centered about our candidate stars.

We simulated a circular patch of sky with $r = 2{,}031''$ (corresponding to a solid angle of 1 deg^2) and populated it with 976 sources randomly distributed within this circular area. Assuming our candidate star was centered on the circular area, we used a circular aperture centered on our stars position (the center of the circular area) and proceeded to count the number of randomly placed sources within our aperture, using an aperture radius from 1″–10″, in steps of 1″. We repeated this process 10^6 times and computed probabilities assuming Poisson statistics for the uncertainties. These probabilities represent the likelihood of having an extragalactic source fall within some radius of our star, assuming extragalactic sources are randomly distributed on the sky. The results of our process are shown in Figure 12, where our probabilities follow a squared power law as expected for circular apertures. Assuming the confusion limit (i.e., the limit at which two objects cannot be distinguished from one) for the $W3$ beam is approximately half of the PSF FWHM (3.25″), then we can estimate the probability for chance alignment with an extragalactic source is $< 0.3\%$. This is a conservative estimate since a source at the confusion limit will appear significantly offset within the *WISE* images, and may also appear as an extended source. If we assume a more likely confusion limit is $< 2''$, this leads to a probability of chance alignment $\lesssim 0.09\%$.

For the computed probabilities to be meaningful, we assessed how many stars in the W11 catalog could have been observed if they had a similar IR excess to our disk candidates. We used a subsample of the W11 catalog that passed the selection criteria outlined in §2.1, not including the *WISE* S/N cuts. We required a magnitude limit to represent the minimal flux detectable by *WISE* at 12 μm; since *WISE* sensitivity is highly dependent upon sky position due to the depth of coverage, we used *WISE* 5σ sensitivity maps[21] to estimate the maximum detectable Vega magnitude for stars in the W11 catalog. Using the sensitivity maps, we estimated a detectable $W3$ Vega magnitude of 13 ± 0.3. The sensitivity maps are based on a noise model, and their flux densities were found to be slightly lower than those produced by external checks, therefore, we used the 1σ limit for our flux density cutoff (i.e., $W3 = 12.7$ or ∼0.24 mJy). For comparison, the minimum $W3$ flux density in our sample was 0.272 mJy.

Since we did not have reliable $W3$ values for the majority of the W11 catalog, we used this value to estimate a minimal detectable flux in another band for which we had information (i.e., $ugrizJHK_s$). We found that J-band magnitudes were good estimators for limiting fluxes due to the fact that the J-band is close to the peak of the SEDs for effective temperatures in the M-spectral type regime (2300–3800 K). We computed J-band magnitudes from synthetic photometry for the range $T_* = 2{,}300$–3,800 K, solar metallicity, $\log(g) = 5$, using stellar radius estimates from Reid & Hawley (2005), at distances between $d = 50$–1,600 pc in steps of 10 pc, representative of the distances within our sample. To determine an appropriate expected IR excess level, we used the average excess within our sample, found to be ∼10 times the photospheric level, and used this value to compute synthetic $W3$ magnitudes for each stellar model to find the corresponding J-band magnitude at the cutoff $W3$ magnitude of 12.7. On average, a J-band magnitude of ∼17 corresponded to a $W3$ magnitude of 12.7 for an excess 10 times the photospheric level. We implemented $J \leq 17$ cutoff, and the resulting catalog contained 41,120 stars that could have been detected in $W3$ with SNR ≥ 3 at the $5\sigma'$ level if they had an equivalent IR excess.

Therefore, for the 41,120 stars that could have a detectable excess, we expect $\lesssim 37$ false positives (0.09% from above). We expect that our visual inspection should have removed many of these, and we will still retain a high number of true detections within our sample. At present, there are no known field M dwarfs ($\gtrsim 1$ Gyr) with IR excess detections. Higher resolution observa-

[21] http://wise2.ipac.caltech.edu/docs/release/allsky/expsup/sec6_3a.html

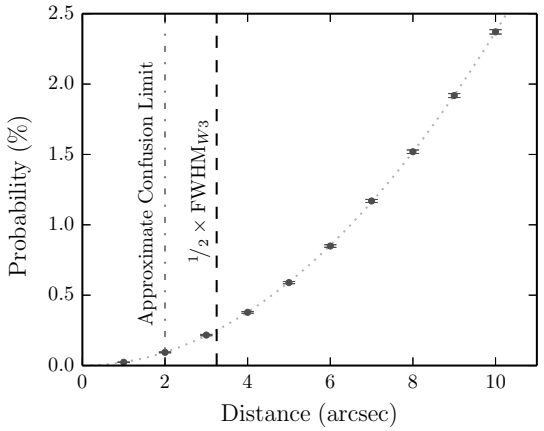

Figure 12. The probability of chance alignment with an extragalactic source as a function of distance. Plotted are the computed probabilities with errors, assuming Poisson statistics, from our Monte Carlo method (circles), and the best-fit squared power law for our probabilities (dotted line). The resolution limit for $W3$ plotted (half of the FWHM, 3.25″; dashed line). The approximate confusion limit is shown as the dash-dotted line (see text).

tions with *JWST* in the future will make it possible to determine how many sources actually have IR interlopers. From our above results, we conclude that most of our observed excesses originate from the M dwarf source, rather than any contaminant.

4. RESULTS

4.1. *Modeling the Dust Population*

If we make the assumption that the excess flux is from a dust population radiating as a blackbody, we can examine the ratio of the dust and stellar luminosity. For our blackbody model fits, we attempted to fit all stars with S/N$_{W4} \geq 2$, excluding stars with *WISE* $W4$ upper limits. We did not fit blackbodies to stars that had only 22 μm flux upper limits since blackbody fits using only 12 μm fluxes are extremely degenerate. We fit 17 of our candidate stars with a single temperature blackbody to model the observed IR excess. This was done using an iterative process where we fit blackbodies with temperatures from 50 to 1,000 K in steps of 5 K, that were added to the flux density from the stellar photosphere, and computed a χ^2 minimization using all photometric bands. We followed a similar process to that outlined in §3, except the newly computed blackbody flux density was normalized to the observed $W4$ flux density rather than the K_s-band. An example of a best-fit dust blackbody is shown in Figure 13.

Fractional luminosities, $L_{\rm dust}/L_*$, can be estimated by taking a ratio of the integrated stellar flux and integrated thermal blackbody flux of the dust. This provides a lower limit to the flux produced by the dust population since there may be more FIR and submillimeter flux produced by colder dust grains. For sources with 12 μm excesses and 22 μm non-detections, we estimated the fractional IR excess with the assumption that $F_{\rm dust} \approx \nu F_\nu$, after subtracting from F_ν the expected stellar flux density contribution. For a thermal body peaking at this frequency, this approximation will typically be ∼74% of the integrated thermal emission. This can be shown in the following approximation:

$$\frac{\lambda_{\rm max} F_{\lambda_{\rm max}}}{\int_0^\infty F_\lambda \, {\rm d}\lambda} = \frac{15 h^4 c^4}{b^4 k^4 \pi^4 (e^{hc/bk} - 1)} \approx 0.736, \quad (3)$$

where k is the Boltzmann constant, c is the speed of light, h is the Planck constant, and b (= 0.0036697 m·K) is the constant found from taking the derivative of λF_λ and solving for the peak value.

In the MIR, we can estimate the fractional luminosity of the dust to the star using the relationship between flux and luminosity, and the fact that disk emission peaks while the stellar flux will be in the Rayleigh-Jeans limit in this wavelength regime. The flux ratio between the dust population and host star becomes:

$$\frac{F_{\rm dust}}{F_*} = \frac{L_{\rm dust}}{L_*} \frac{hcT_*^3}{\lambda k T_{\rm dust}^4 (e^{hc/\lambda k T_{\rm dust}} - 1)}. \quad (4)$$

The minimum fractional luminosity for our stars with only 12 μm excesses can be simplified assuming the peak emission is at 12 μm (corresponding to $T_{\rm dust} \approx 306$ K):

$$\frac{L_{\rm dust}}{L_*}({\rm minimum}) = 10^{-2} \left(\frac{3304\,{\rm K}}{T_*} \right)^3 \frac{F_{12,\,{\rm dust}}}{F_{12,\,*}}. \quad (5)$$

Fractional luminosities are listed in Table 5.

We find that many of our stars exhibit large fractional luminosities (∼10^{-2}–10^{-1}), approximately five orders of magnitude larger than estimates of the Kuiper belt's luminosity relative to the Sun (Beichman et al. 2005). This is also larger than values typically associated with debris disks ($L_{\rm dust}/L_* \sim 10^{-3}$; Rebull et al. 2008). Gautier et al. (2008) observed similar fractional luminosities for low-mass stars in η Chamaeleontis, a young (4–15 Myr; Mamajek et al. 2000; Luhman 2004; Lyo et al. 2004) stellar association. Fractional luminosities $> 10^{-2}$ have been observed around both classical T Tauri stars (CTTSs) and weak-line T Tauri stars (WTTS) (Padgett et al. 2006; Cieza et al. 2007), however, the majority of stars in our sample exhibit no Hα emission, and are therefore likely older than 1 Gyr. We will discuss the implications of this in §5.

We can further characterize the dust population if we assume it exists in radiative equilibrium with the host star. For a dust grain in radiative equilibrium with its host star, the distance from the host star is given by:

$$D = \frac{1}{2} \left(\frac{T_*}{T_{\rm gr}} \right)^2 R_*, \quad (6)$$

(Jura et al. 1998; Chen et al. 2005). Here T_* and $T_{\rm gr}$ are the stellar effective temperature and dust grain temperature, and R_* is the stellar radius. For stars without 22 μm excesses we assumed $T_{\rm gr} \approx 306$ K, the radiative temperature of a blackbody at 12 μm. The average distance was calculated to be ∼0.16 AU for the combined sample, within the snow line for planets around M dwarfs (∼0.3 AU; Ogihara & Ida 2009). Minimum distances are listed in Table 5.

Fractional IR luminosities can be used to estimate a dust mass if we make a few assumptions. First, we assume an average grain radius, a, and density, ρ_s. For reasons we will discuss in §5, we assume the IR excesses we are viewing are due to planetary collisions rather

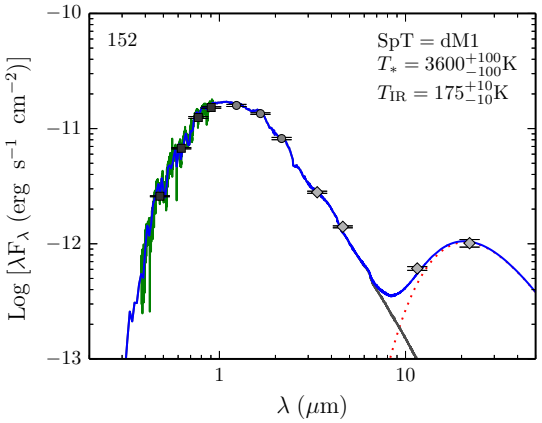

Figure 13. A sample SED for one of the 17 stars with its IR excess fitted with a single temperature blackbody. Plotted are SDSS photometry (squares; *u*-band omitted due to large uncertainties for cool stars), 2MASS (circles), and *WISE* (diamonds), along with SDSS spectra (green). The catalog number is listed in the upper left. The best-fit combined model is plotted in blue, along with each of the model components (photosphere in gray, dust blackbody as dashed red line). Source spectral type, model effective temperature, and blackbody temperature are listed in the top right hand corner of each panel. SEDs for the entire sample are available online.

than primordial dust content; then, using the results of Weinberger et al. (2011), we assumed an average minimum grain size of $\langle a \rangle = 0.5$ μm, noting that particles can have $a > 10$ μm. Grain size plays an important role in the observations, since larger grains, which radiate more efficiently, will show similar temperatures at closer orbital distances to smaller grains at larger orbital distances. Therefore, we used 0.5 μm as a lower limit similar to Weinberger et al. (2011), noting that larger grains, which put dust populations closer to their host stars, do not change the results of our discussion (§5). We assumed a typical grain density of $\rho_s = 2.5$ g cm^{-3} (Pollack et al. 1994). If we assume the dust is in a thin shell, orbiting a distance D from the host star, with a particulate radius a and density ρ_s, and a cross-section equal to the physical cross section of a spherical grain, we can define the dust mass as:

$$M_d \geq \frac{16}{3}\pi \frac{L_{\rm dust}}{L_*} \rho_s \langle a \rangle D^2_{\rm min}, \quad (7)$$

(Chen et al. 2005). Our computed dust masses are listed in Table 5. A few of our stars have dust masses on the order of AU Mic's ($10^{-4} M_{\rm moon}$; Chen et al. 2005). However, a typical disk mass in our sample is comparable to, if not slightly larger than, those observed for debris disks ($10^{-5} M_{\rm moon}$). IR spectra of these systems will help to further characterize and constrain the crystallinity of the dust content, similar to the methods used in Weinberger et al. (2011). In particular, IR spectra may be useful to distinguish dust produced from planetary collisions within the terrestrial zone versus primordial dust. This will be discussed further in §5.

4.2. *Spectral Signatures of Youth*

Low-mass stars not only have extremely long main sequence lifetimes, they have long pre-main sequence lifetimes, from 100s of Myrs to over a Gyr dependent on mass (Baraffe et al. 2002). Disk lifetimes around low-mass stars are not well constrained; some theories predict that low-mass stars can retain their disks for periods much longer than that for solar-type stars (∼10 Myr; Plavchan et al. 2009). For comparison, the 12 Myr AU Mic (dM1e; Wilner et al. 2012) has shown excess at both 22 μm (A12) and 70 μm (Plavchan et al. 2009). Therefore, youth is important to quantify to help inform the timescale for disk dispersal.

Most of our disk candidates appear to be field stars, not affiliated with any known star-forming region or young stellar association. However, there remains the possibility that some of the stars in our sample are members of unknown young stellar associations or moving groups, or unidentified members of known associations. To test for youth within our sample, we looked at tracers of surface gravity, magnetic activity, and lithium absorption. Youth was quantified through an index for each tracer measured. These indices are listed in Table 6.

4.2.1. *Surface Gravity*

Pre-main sequence stars that are still contracting onto the main sequence will exhibit weaker surface gravity relative to stars on the main sequence. Several atomic/molecular bands have been identified as reliable tracers of surface gravity. To estimate surface gravities for our sample, we analyzed the atomic alkali lines of Na I (8183 and 8195 Å) and K I (7665 and 7699 Å) identified in Slesnick et al. (2006), and the CaH 3 molecular absorption band from Reid et al. (1995). Other studies of nearby, young low-mass stars have used these same molecular features as proxies for youth (e.g., Shkolnik et al. 2009, 2011, 2012; Schlieder et al. 2012a).

One caveat to using molecular bands as a diagnostic for surface gravity is their dependence on stellar metallicity. We can interpret the findings of Woolf & Wallerstein (2006) to surmise that higher metallicity will increase both the Na I and K I equivalent width (EW) measurements. Therefore, a star with low surface gravity and high metallicity may appear to have high surface gravity. Metallicities are difficult to measure for low-mass stars due to their large abundance of molecular features and incomplete line lists. Many studies attempted to find metallicity tracers using methods both photometric (Bonfils et al. 2005; Johnson & Apps 2009; Schlaufman & Laughlin 2010) and spectroscopic (Lépine et al. 2007; Rojas-Ayala & Lloyd 2010; Terrien et al. 2012; Mann et al. 2013; Newton et al. 2014). We employed the methods outlined in Mann et al. (2013) to determine metallicity using the SDSS spectra (§4.4). We find that the majority of our stars appear to have solar metallicity, and should not affect our gravity sensitive spectroscopic features excessively. Considering this we used a comparative approach for estimating surface gravities.

The CaH 3 index was computed following the method outlined in Reid et al. (1995). Line measurements were made by integrating over a specific width centered on each line, and subtracting off the mean flux calculated from two adjacent continuum regions; regions are listed in Table 7. EWs were computed for each line by dividing the integrated line flux by the mean continuum value. Formal EW uncertainties for each line were also computed. We integrated the Na I doublet over a sin-

Table 6
Spectral Measurements

Catalog Number	Hα EW (Å)	K I EW[a] (Å)	Na I EW[b] (Å)	CaH 3[c]	TiO 5[c]	Youth Index[d]
40.....	-2.78 ± 0.22	2.07 ± 0.11	1.71 ± 0.09	0.81 ± 0.01	0.61 ± 0.01	1010
42.....	-5.09 ± 0.23	2.13 ± 0.10	2.24 ± 0.07	0.77 ± 0.01	0.56 ± 0.01	1110
62.....	-6.82 ± 1.03	7.28 ± 0.74	5.91 ± 0.36	0.66 ± 0.03	0.33 ± 0.03	1100
78.....	-11.21 ± 1.07	8.72 ± 1.13	5.24 ± 0.34	0.56 ± 0.03	0.29 ± 0.03	1000
108.....	0.03 ± 0.07	1.99 ± 0.13	2.31 ± 0.13	0.85 ± 0.01	0.74 ± 0.01	0000
110.....	-0.05 ± 0.21	2.96 ± 0.35	4.06 ± 0.29	0.74 ± 0.03	0.48 ± 0.03	0000
115.....	0.55 ± 0.11	1.71 ± 0.21	2.33 ± 0.21	0.85 ± 0.02	0.76 ± 0.03	0000
126.....	0.21 ± 0.15	3.03 ± 0.31	1.85 ± 0.26	0.85 ± 0.03	0.68 ± 0.03	0000
140.....	-84.02 ± 16.83	4.35 ± 0.38	3.39 ± 0.14	0.70 ± 0.01	0.41 ± 0.01	1000
142.....	0.36 ± 0.08	1.24 ± 0.18	1.61 ± 0.15	0.88 ± 0.02	0.80 ± 0.02	0000
152.....	0.14 ± 0.04	1.93 ± 0.09	1.56 ± 0.08	0.85 ± 0.01	0.64 ± 0.01	0001
156.....	0.30 ± 0.35	2.05 ± 0.59	...	0.77 ± 0.05	0.69 ± 0.06	0000
164.....	0.30 ± 0.08	1.98 ± 0.16	1.62 ± 0.16	0.89 ± 0.01	0.81 ± 0.02	0000

Note. — Values listed only for stars with $SNR_{W4} \geq 3$. Values for the combined sample are available online. Negative EWs indicate emission.

[a] K I doublet (7665 & 7699 Å).

[b] Na I doublet (8183 & 8195 Å).

[c] Defined in Reid et al. (1995).

[d] Youth index: Hα emission, low surface gravity in at least 2 of the 3 tracers (§4.2.1), lithium absorption, and UV activity.

Table 7
Line Measurement Regions

Line	Central λ (Å)	Width (Å)	Continuum A (Å)	Continuum B (Å)
Na I	8189	22	8149–8169	8236–8258
K I a	7665	16	7651–7661	7680–7690
K I b	7699	16	7680–7690	7710–7720

Note. — All of the wavelengths are given in vacuum units.

gle region, and summed two separate regions for the K I doublet.

We expect the majority of stars in the W11 catalog to be older field dwarfs. Therefore, to determine low surface gravity members of our sample, we compared gravity tracers for our sample relative to the W11 catalog. We grouped stars by spectral type and determined quartiles for each gravity tracer and spectral type bin. We plot our surface gravity tracers in Figure 14, compared to the W11 catalog. We expect low surface gravity members of the W11 catalog to appear as outliers in each gravity tracer within each spectral type bin. The majority of the stars in our sample fall within the intrinsic scatter of the W11 catalog (between the 1st and 3rd quartiles), indicating that we are observing an older stellar population rather than pre-main sequence stars. Each star that shows lower surface gravity relative to the W11 quartiles (i.e., below the 1st quartile for Na I and K I, or in the 4th quartile for CaH 3) in at least two of the three tracers has been marked in Table 6. Overall, the combined sample does not appear to have significantly lower surface gravities over the W11 catalog, however, the Orion candidates either fall below or straddle the lower end of the W11 catalog quartiles for each surface gravity tracer, implying that it is likely a younger stellar population.

For our sample we computed the percentages of stars with surface gravities lower than the W11 3rd quartiles, and lower than the W11 medians, respectively; values are listed in Table 8. The combined sample has only a small percentage of low-surface gravity stars (< 15%). The large percentage of stars with low-surface gravity towards Orion indicates that these stars are probably members of the star-forming region rather than field stars along the LOS. These stars will be discussed further in §4.6.

Table 8
Surface Gravity Statistics

Sample	# of Stars with log(*g*) < W11 3rd Quartile	W11 Median
Combined	17.7%	47.4%
Combined w/o Orion	14.9%	45.2%

4.2.2. *Lithium Absorption*

Young pre-main sequence M dwarfs that are still contracting onto the main sequence rapidly destroy their natal lithium content as their interiors reach the required temperature ($\sim 2.5 \times 10^6$ K). Once they have contracted onto the main sequence, an early-type M dwarf will deplete its lithium by a factor of 2 in less than 10 Myr, whereas a late-type M dwarf may show absorption at ∼100 Myr (Cargile et al. 2010). In addition, fully convective stars ($M \lesssim 0.35 M_\odot$; Chabrier & Baraffe 1997) that exhibit episodic accretion can increase the rate of lithium depletion by increasing central temperatures, with complete lithium depletion occurring between 10 to a few 100 Myr in models (Baraffe & Chabrier 2010). Therefore, measuring the lithium feature (Li I 6708 Å) provides a strong youth tracer.

Due to the low S/N around the Li I feature, and the strong TiO bands in close proximity, a direct measurement of this feature was not attempted. Instead, we decided to compare our spectra to the template spectra from Bochanski et al. (2007b). Bochanski et al. (2007b) created template spectra through co-addition of ∼ 4,300 high S/N SDSS spectra of field M dwarfs. These template spectra represent a statistically older population of M dwarfs, with little to no lithium absorption in their spectra. Comparing these template spectra to our sample SDSS spectra, we can identify significant lithium deple-

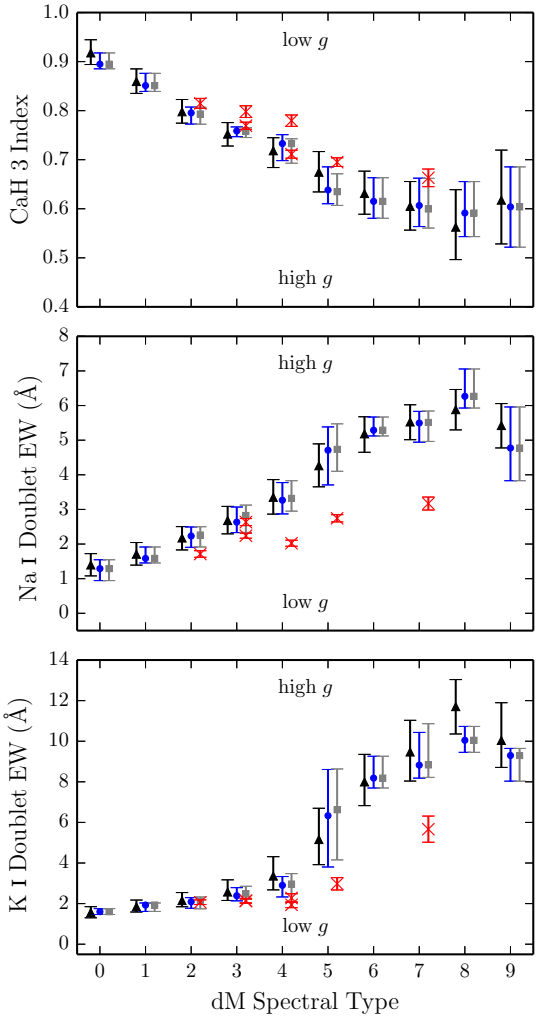

Figure 14. Log(g) tracers for the combined sample (blue circles), the combined sample without the Orion candidates (gray squares), Orion candidates (red crosses), and the W11 catalog (black triangles). All data points represent the median value with error bars representing the 1st and 3rd quartiles for each spectral type, except for the Orion candidates which show actual measurements and uncertainties. As an ensemble, the combined sample does not appear to have characteristically lower surface gravities compared to the W11 catalog, however, the Orion candidate stars appear to have low-surface gravity relative to the W11 values (see Table 8).

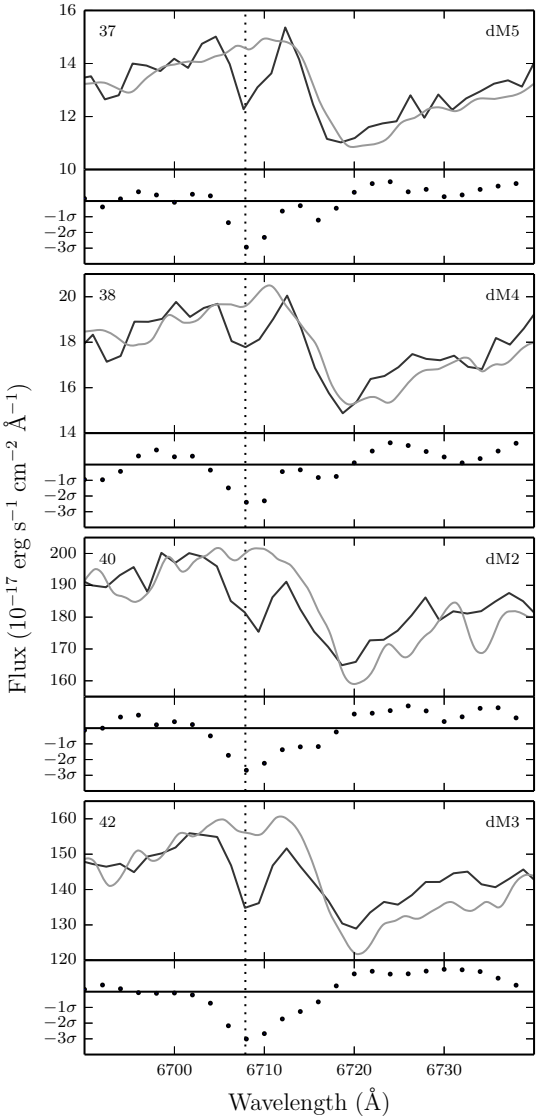

Figure 15. Spectral profiles (dark gray line) for stars in the combined sample showing lithium absorption at 6708 Å (dotted line). SDSS template spectra from Bochanski et al. (2007b) are plotted for comparison (light gray line). Below each spectra are the moving integrated residuals showing Li absorption. The template spectra represent older field dwarfs ($\gtrsim$1 Gyr) with little to no absorption. Catalog number and spectral type are listed in the top left and right corner, respectively.

tion in comparison to the template to identify stars that are younger than average field stars. To determine the significance of the absorption feature, we used a method similar to that in Cargile et al. (2010), using a moving integrated residual. The moving integrated residuals were determined by integrating over the residuals from the template spectrum minus the SDSS spectrum in a moving 5 Å window. This window was moved in steps of 2 Å. Using the moving window, small differences between the template and source spectrum are averaged out, providing a better measure of the deviations between the two. Standard deviations are derived from the R.M.S. of the residual outside a 10 Å window that is centered at 6708 Å. For further details on this method see Cargile et al. (2010).

We applied the Cargile et al. (2010) method on every star in our sample and found four of the 175 had a detectable amount of lithium. The method can be seen in Figure 15, where we display the four stars in our sample showing significant lithium absorption relative to the template spectra. These stars are marked in Table 6 and all four are found in the Orion footprint. Due to the assumed ages of field stars within the W11 catalog ($\gtrsim$ 1 Gyr), we would expect none of these stars to show detectable amounts of lithium if they are members of the field. Although we make no attempt to assign ages to these stars, it is probable that they are not members of the field and are younger stars associated with the Orion OB1 association.

4.2.3. *Hα Emission*

Over the past few decades, numerous studies have linked magnetic activity (traced through hydrogen emis-

sion) to stellar age (e.g., Wilson 1963; Skumanich 1972; Eggen 1990; Soderblom et al. 1991; Hawley et al. 1996, 2000). W08 found that for M dwarfs with spectral types earlier than dM4, the average activity lifetime was less than 2.5 Gyrs, increasing to as long as 8 Gyrs for stars with spectral types later than dM4. Although the assumed primordial disk dispersal time is far shorter than the activity lifetime for any M dwarf (10s of Myrs versus Gyrs), Hα provides another diagnostic that we can use to differentiate a statistically younger population from an older one, particularly for stars with spectral types earlier than dM4. Hydrogen transitions have also been observed as a sign of accretion, with an increase in line width measurements over typical magnetically active stars (White & Basri 2003).

Using the RVs computed in this study, we remeasured the hydrogen Balmer transitions following the methods outlined in W11 to analyze the magnetic activity within our sample. Stars were flagged as active (ACTHA = 1) if they met the following criteria: the Hα equivalent width (EW) < 0.75 Å, the S/N in the continuum was greater than three, the EW value was three times the uncertainty, and the height of the spectral line was larger than three times the noise in the continuum. The small size of our sample allows us to visually inspect each spectrum to make sure the activity flag corresponded to a real signal, and did not potentially miss stars that exhibited Hα emission. We found all stars flagged as active to show some amount of Hα emission visible in the SDSS spectrum, with none of the stars flagged as inactive showing emission. Hα EW measurements are listed and active candidates are marked in Table 6.

To compare the level of activity in our sample to a relatively unbiased sample of field stars, we computed activity fractions ($N_{\rm active}/N_{\rm total}$) for each spectral type bin and compared them to the W11 values. We define stars as active using the same criteria as W11. For the total number of stars, we only used stars that were defined as active or inactive (using the W11 criteria), omitting stars that did not have high enough S/N to categorize their activity status. Figure 16 shows the activity fractions for stellar samples from this study versus the W11 catalog. The number of stars that went into each bin are listed in Table 9. Although our small sample size makes it difficult to draw strong conclusions, we can see that activity fractions are not significantly different between our sample and the W11 catalog. If we remove the Orion candidates from our combined sample, activity fractions drop for each spectral-type bin that contains Orion candidates. This suggests that the majority of "young" stars in our sample are the Orion candidates, giving additional weight to the possibility that those stars are indeed members of the Orion OB1 association. Considering the long activity lifetimes for low-mass stars, the majority of our combined sample do not show characteristics of a young stellar population (< 100 Myr). If our stellar sample is older than $\sim$1 Gyr, this suggests that either the IR excesses we observe do not result from primordial circumstellar material, or that the disk dispersal time for low-mass stars can last for much longer than current theories and empirical data predict (10s of Myrs). Further discussion of interpretations for these IR excesses will ensue in §5.

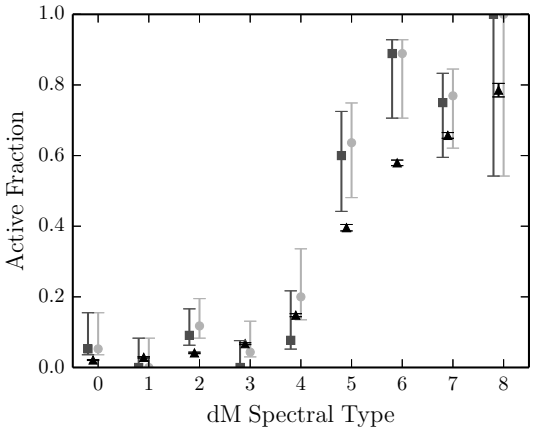

Figure 16. Activity fractions for stars from the combined sample (circles), the combined sample without the Orion candidates (squares), and the W11 catalog (triangles). The error bars represent binomial distribution errors. Without the Orion candidates, the combined sample typically has lower activity fractions than the W11 catalog, implying the Orion candidates are mostly younger, active stars. As an ensemble, we do not see significantly different activity fractions between the W11 catalog and our combined sample.

4.2.4. *Ultraviolet Flux*

Heating of the chromosphere also produces ultraviolet (UV) emission through a number of transitions (Linsky et al. 2001; Findeisen & Hillenbrand 2010), which provides another tracer for stellar activity, and hence youth. Included in the UV emission spectrum are the Mg II resonance lines, a host of Fe II lines, and other species including: Lyα, C II, Al II, C III, Si III, Si IV, and He II (Walkowicz et al. 2008; France et al. 2012). Shkolnik et al. (2011) determined criteria to separate older populations from young populations of M dwarfs using the *Galaxy Evolution Explorer* (*GALEX*; Martin et al. 2005) near ultra-violet (NUV, 1750–2750 Å) and far ultra-violet (FUV, 1350–1750 Å) fluxes.

Using a cross-matched catalog between *GALEX* Data Release 6 sources and the W11 catalog (Jones & West 2014, in preparation), we found five matches to our sample that had flux measurements in the NUV, FUV, or both. The fraction of our sample (2.9%) matched to *GALEX* sources that had either an NUV or FUV detection is comparable to the fraction of sources Jones & West (2014, in preparation) were able to match to the entire W11 catalog (1.4%). Due to the distances to stars in the W11 catalog ($d \gtrsim 100$ pc), UV emission from *inactive* M dwarfs should be undetectable (Jones & West 2014, in preparation). None of the matched *GALEX* objects were associated with any of our Orion stars.

To determine M dwarfs showing significant UV flux as a tracer for stellar activity, Shkolnik et al. (2011) compared *GALEX* fluxes to 2MASS J-band fluxes to separate young, active stars from quiescent, older stars and white dwarf/M dwarf close binaries. One of the stars in our combined sample had both NUV and FUV fluxes, and significant fractional UV fluxes ($F_{\rm NUV}/F_J \approx F_{\rm FUV}/F_J > 10^{-4}$), and is flagged in Table 3. All five stars that showed NUV flux, independent of whether they had a FUV detection, show significant NUV excess ($F_{\rm NUV}/F_J \gtrsim 10^{-4}$). We would expect stars showing strong UV flux to exhibit other chromospheric heating

Table 9
Activity Indicators

SpT	$N_{\rm active}$	$N_{\rm inactive}$	Active Fraction	$N_{\rm active}$	$N_{\rm inactive}$	Active Fraction	$N_{\rm active}$	$N_{\rm inactive}$	Active Fraction
	Combined Sample			Combined Sample w/o Orion			West et al. (2011) Catalog		
M0	1	18	$0.05^{+0.10}_{-0.02}$	1	18	$0.05^{+0.10}_{-0.02}$	207	9573	$0.02^{+0.01}_{-0.01}$
M1	0	20	$0.00^{+0.08}_{-0.01}$	0	20	$0.00^{+0.08}_{-0.00}$	226	7649	$0.03^{+0.01}_{-0.01}$
M2	4	30	$0.12^{+0.08}_{-0.03}$	3	30	$0.09^{+0.08}_{-0.03}$	366	8496	$0.04^{+0.01}_{-0.01}$
M3	1	22	$0.04^{+0.09}_{-0.01}$	0	22	$0.00^{+0.08}_{-0.00}$	623	8630	$0.07^{+0.01}_{-0.01}$
M4	3	12	$0.20^{+0.14}_{-0.07}$	1	12	$0.08^{+0.14}_{-0.02}$	1040	5983	$0.15^{+0.01}_{-0.01}$
M5	7	4	$0.64^{+0.11}_{-0.16}$	6	4	$0.60^{+0.12}_{-0.16}$	1143	1745	$0.40^{+0.01}_{-0.01}$
M6	8	1	$0.89^{+0.04}_{-0.18}$	8	1	$0.89^{+0.04}_{-0.18}$	2288	1661	$0.58^{+0.01}_{-0.01}$
M7	10	3	$0.77^{+0.08}_{-0.15}$	9	3	$0.75^{+0.08}_{-0.16}$	2236	1167	$0.66^{+0.01}_{-0.01}$
M8	2	0	$1.00^{+0.01}_{-0.46}$	2	0	$1.00^{+0.01}_{-0.46}$	362	99	$0.79^{+0.02}_{-0.02}$

signs, however, only one of the five stars exhibit Hα emission or any other youth tracer. Shkolnik et al. (2011) estimate the probability of flaring M dwarfs contributing to *GALEX* source counts to be $< 3\%$, therefore, although unlikely, it is possible *GALEX* observed these stars during flare activity.

4.3. *Kinematics*

Stellar kinematics can provide additional insight into the age of a stellar population. To closely examine the kinematics of our stars, we used the USNO-B/SDSS proper motions (Munn et al. 2004, 2008), radial velocities computed in this study, and photometric parallax distances to compute UVW space motions. UVW velocities are in a right-handed Cartesian coordinate system, representing motion towards the Galactic center, motion in the direction of the Sun's motion, and motion northwards away from the Galactic plane, respectively. For stars at appreciable distances, UVW velocities may not be appropriate tracers of Galactic motion, however, the vast majority of our stars are within the distance limits used by other studies of stellar kinematics ($d < 1{,}600$ pc, $|Z| < 1{,}000$ pc; Bochanski et al. 2007a). Younger stars will typically have small UVW motions with respect to the local standard of rest (LSR), with older stellar populations lagging the LSR along the direction of galactic rotation (V component), a phenomenon known as "asymmetric drift" (Strömberg 1922, 1925).

UVW velocities and uncertainties were computed following the method of Johnson & Soderblom (1987) by way of a Python version of the IDL procedure `gal_uvw.pro`. These values were then corrected for the solar motion ($U = 11.1$ km s^{-1}, $V = 12.24$ km s^{-1}, $W = 7.25$ km s^{-1}; Schönrich et al. 2010) with respect to the LSR. The kinematics of our samples are shown in Figure 17. As an ensemble, our stars appear to have kinematics typical of the disk population (Leggett 1992). The Orion candidates appear to be distributed about the origin of velocity space, indicating a younger stellar population. There also appears to be five stars with velocities on the order of, or larger than, the escape velocity of the Galaxy ($\sim$400–500 km s^{-1}; Piffl et al. 2014).

Older stellar populations will have been dynamically heated over time, causing a larger velocity dispersion as a population. As is shown in Figure 17, our Orion candidates have narrow UVW velocity distributions compared to our combined sample, indicating a younger, less dynamically heated stellar population. We can also see the skew of the V distribution for our combined sample to more negative values, indicative of asymmetric drift. There are a few outliers in our Orion velocity distributions, most likely due to field stars along our line of sight. We do not perform an in-depth investigation on the candidacy of these stars here, although one is warranted. The computed average and dispersion of the UVW components for our combined sample without the Orion candidates, as listed in Table 10, are similar to other studies of late-type stars (Fuchs et al. 2009). We acknowledge that there is a selection bias due to the fact that we cannot probe the motions of stars in the distant Galaxy, where stellar motions are different due to the age of those stellar populations, however, this should not significantly affect our analysis of the Orion candidates.

Five of our stars showed high velocity kinematics, usually associated with "hypervelocity" or runaway stars. The largest component of motion for these stars is tangential to our line of sight, therefore, we needed to make sure our proper motions were reliable. All five high proper motion stars passed the quality cuts defined in Kilic et al. (2006, SIGRA < 525, SIGDEC < 525), which were an extension of the cuts defined by Munn et al. (2004). They were also found in multiple proper motion catalogs, and values are listed in Table 11. These stars may be a population of runaway stars, representing some of the first sub-solar hypervelocity stars found to date (Palladino et al. 2014). An in-depth study of these stars is beyond the scope of this work, however, a number of these stars will be discussed further in the kinematical study of high-velocity M dwarfs by Favia & West (2014, in preparation). We will discuss scenarios that could explain an IR excess for a star moving with a high velocity relative to the ISM in §5. USNO-B/SDSS proper motions and our derived kinematics for all our stars are available in the online catalog.

4.4. *Metallicity*

There is evidence that metallicity plays a vital role in the formation of stars and planets. Metallicity has been shown to correlate with the rate of giant planet occurrence (Gonzalez 1997; Fischer & Valenti 2005; Johnson et al. 2010; Mann et al. 2012). Studies of nearby clusters have shown that metal rich environments

Table 10
Velocity Components

Sample	$\langle U \rangle$	$\sigma_{\langle U \rangle}$	$\langle V \rangle$	$\sigma_{\langle V \rangle}$	$\langle W \rangle$	$\sigma_{\langle W \rangle}$
Combined w/o Orion Candidates	10.19 ± 2.83	29.70	-11.98 ± 2.78	29.12	0.59 ± 2.03	21.31
Orion Candidates	20.52 ± 2.71	7.18	8.89 ± 6.01	15.90	10.64 ± 0.84	2.23

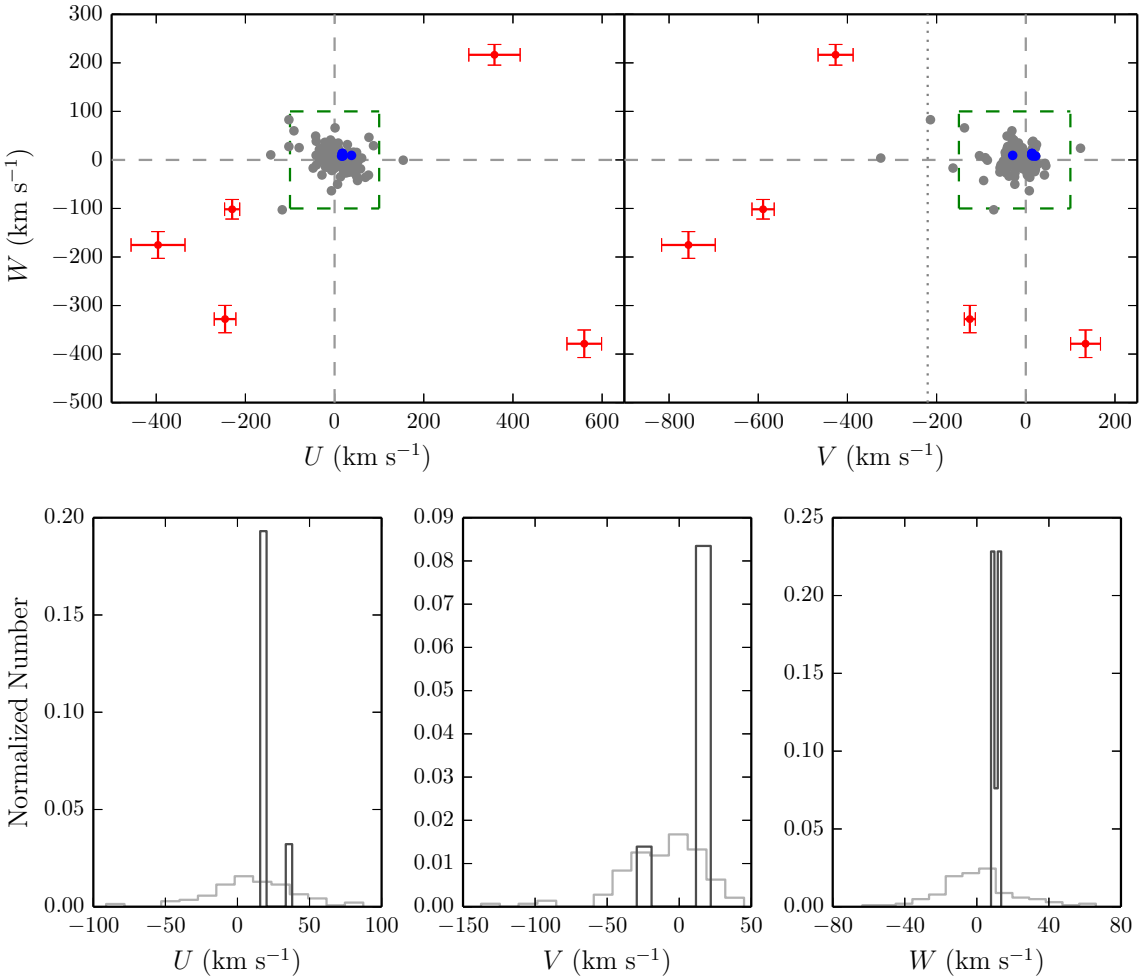

Figure 17. Stellar kinematics for stars with good proper motions (GOODPM = 1). Top: The combined sample (gray points) with high velocity stars marked ($v_{\rm tot} > 400$ km s^{-1}; red crosses). Orion stars are plotted as blue points. The majority of stars appear to have kinematics typical of the disk population, with a few exhibiting lagging V velocity components, expected from older M dwarfs (see text for details). The dotted line is drawn at $V = -220$ km s^{-1}, separating stars which are moving along the direction of Galactic rotation from stars moving counter to it. Bottom: Normalized velocity distributions for stars that fall within the green dashed line for our combined sample minus the Orion candidates (light gray) and Orion candidates (dark gray). The Orion candidates show far less dispersion in their UVW velocities, indicating a younger dynamical population. The tail of the distribution shown in the Orion candidates indicates there may be a few field stars along our line of sight. The largest source of error for the high velocity stars are the photometric distance errors, which may be ∼20–30% of the distance measurement.

may allow primordial circumstellar disks to persist on longer timescales (Yasui et al. 2009, 2010). Additionally, accretion of planetary bodies may increase the metallicity of the host star (e.g., Farihi et al. 2009). Therefore, a detailed understanding of how metallicity affects disk evolution is crucial to understanding stellar and planetary system formation and evolution.

It is challenging to measure the metal content of M dwarfs due to their large abundance of molecular features, many of which have incomplete line lists. Previous studies have attempted to find metallicity tracers using both photometric (Bonfils et al. 2005; Johnson & Apps 2009; Schlaufman & Laughlin 2010), and spectroscopic methods (Lépine et al. 2007; Rojas-Ayala & Lloyd 2010; Dhital et al. 2012; Mann et al. 2012; Önehag et al. 2012; Rojas-Ayala et al. 2012; Terrien et al. 2012; Newton et al. 2014). Recently, Mann et al. (2013) completed an investigation of metallicity sensitive tracers in the optical and NIR spectra of late K and M dwarf companions to higher mass stars. The Mann et al. (2013)

Table 11
High Velocity Candidate Kinematics

Parameter	Reference	Candidate 27	Candidate 50	Candidate 73	Candidate 106	Candidate 125
$\mu_{\rm R.A.}$ (mas yr^{-1})	Munn et al. (2004, 2008)	-349.5 ± 17.1	-24.6 ± 3.4	-185.1 ± 3.0	-65.9 ± 3.4	262.1 ± 2.9
	Monet et al. (2003)	-352 ± 43	-22 ± 9	-192 ± 6	-62 ± 2	266 ± 4
	Lépine & Shara (2005)[a]	...	...	-192 ± 7	-70 ± 7	235 ± 7
	Roeser et al. (2010)	-346.5 ± 16.2	-27.4 ± 4.3	-191.9 ± 4.2	-67.5 ± 4.3	266.3 ± 3.7
	Salim & Gould (2003)	...	...	-189.4 ± 5.5	...	...
$\mu_{\rm Dec.}$ (mas yr^{-1})	Munn et al. (2004, 2008)	-212.2 ± 17.1	-87.6 ± 3.4	-159.8 ± 3.0	-145.5 ± 3.4	-85.4 ± 2.9
	Monet et al. (2003)	-230 ± 39	-80 ± 7	-152 ± 4	-140 ± 3	-80 ± 3
	Lépine & Shara (2005)[a]	...	...	-170 ± 7	-150 ± 7	-87 ± 7
	Roeser et al. (2010)	-236.6 ± 16.2	-91.1 ± 4.3	-160.9 ± 4.2	-150.8 ± 4.3	-87.1 ± 3.7
	Salim & Gould (2003)	...	...	-156.95 ± 5.5	...	...
RV (km s^{-1})		-5.5 ± 6.7	97.1 ± 8.9	-50.7 ± 4.6	-51.1 ± 5.0	-129.0 ± 2.4
U (km s^{-1})		558.8 ± 38.8	-230.8 ± 16.9	-397.0 ± 60.5	357.5 ± 57.6	-246.7 ± 24.3
V (km s^{-1})		127.0 ± 33.5	-596.1 ± 24.9	-763.5 ± 60.2	-433.5 ± 39.3	-132.5 ± 12.4
W (km s^{-1})		-378.8 ± 28.4	-101.7 ± 20.2	-175.3 ± 27.6	216.5 ± 21.3	-328.0 ± 28.1
$v_{\rm tot}$ (km s^{-1})		689.1 ± 35.8	640.5 ± 23.9	871.7 ± 59.3	597.9 ± 45.2	428.5 ± 25.9

[a] Typical uncertainties stated.

metallicity solutions are comprised of a set of equations based on equivalent widths and color indices. A number of metal sensitive features were found, including Na I (doublets at 8200 Å and 2.208 μm), Ca I (1.616 μm and 1.621 μm), and K I (1.5176 μm), many of which were previously known to be metal sensitive.

To study the metallicity of our sample, we used the SDSS spectra to compute equivalent widths and color indices in line with the methods defined in Mann et al. (2013). To balance quality measurements with a statistically significant sample size, we used only stars with $\sigma_{\rm [Fe/H]} < 0.5$ for our analysis, however, cutting on lower or higher values of $\sigma_{\rm [Fe/H]}$, or removing the Orion candidates, did not significantly change our results. We find our sample to be distributed about solar metallicity, with a median value of [Fe/H] $\approx -0.03 \pm 0.28$, as shown in Figure 18. This is similar to values computed for the W11 catalog ([Fe/H] $\approx -0.02 \pm 0.10$) using the same quality cut of $\sigma_{\rm [Fe/H]} < 0.5$. For the scenario of tidal disruption and accretion of minor planets, we might expect our stars to be preferentially metal rich due to accretion, similar to results observed for white dwarfs with IR excesses (Jura 2003, 2008; Farihi et al. 2009). However, for our stars we do not see a trend of high metallicity, making the tidal disruption and accretion scenario unlikely. Our stars do not have a significantly different metallicity distribution from the W11 catalog (as inferred by a K-S test; p-value = 0.57), therefore, we can draw no obvious conclusions about the metal content affecting, or being affected by, the mechanism for the observed IR excesses.

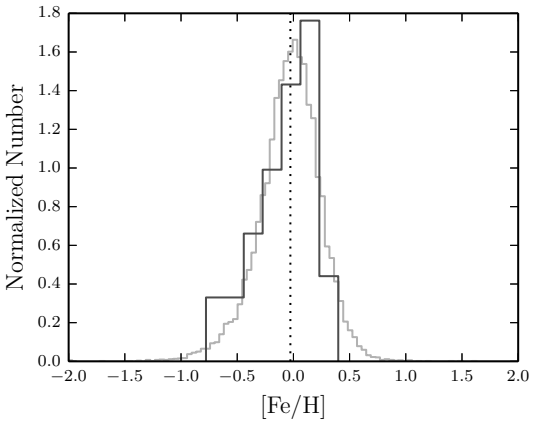

Figure 18. The normalized distribution of [Fe/H] measurements. We show stars from our combined sample (dark gray line) and the W11 catalog (light grey line) with $\sigma_{\rm [Fe/H]} < 0.5$. Measurements were made using the method described in Mann et al. (2013). Only stars with a SpT < dM7 were used. The median for the our sample is shown ([Fe/H] $\approx -0.03 \pm 0.28$; dotted line). Our disk candidates appear to be distributed fairly evenly about solar metallicity, and appear to have a similar distribution to that of the W11 catalog. Dust caused from accretion of minor planets has been shown to increase the metal content of white dwarfs, however, no similar trend is seen here.

4.5. *Disk Fractions*

Our combined sample is large enough to study the nature of the excess IR flux in a Galactic context. Young star forming HII regions are found most prominently in spiral arms, close to the Galactic plane. For example, Lee & Lim (2008) found that ∼90% of embedded clusters are found within ∼160 pc of the Galactic plane. Therefore, we should expect young populations of stars to appear close to the Galactic plane with the number dropping off with vertical Galactic height. This "Galactic stratigraphy" was used in W08, using magnetic activity as a proxy for youth. W08 found that the fraction of active M dwarfs declined with Galactic height, with different slopes for different spectral types, most likely due to the correlation between activity lifetime and spectral type. To test for a similar trend in our data, we performed a "Galactic stratigraphy" analysis to investigate any age dependence for the observed IR excesses.

Using our catalog of 41,120 stars for which we could have observed an IR excess (§3.2.2), we computed the fraction of stars with disks as a function of Galactic height. Figure 19 shows the fraction of disks (using $W3$ excess as a proxy), as a function of distance from the Galactic plane. Once the Orion candidates are removed, we see a fairly constant fraction until a distance of ∼700 pc, at which point we see a slight decline. Separating stars by spectral type does not change this result. As each Galactic height bin represents an ensemble of young and old stars, with younger stars more preferentially found closer to the plane, we surmise that the mech-

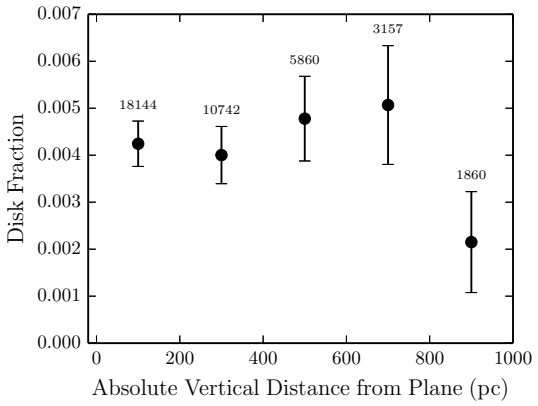

Figure 19. Disk fractions (using $W3$ excess as a proxy) as a function of height using the combined sample without the Orion candidates. Error bars represent binomial errors. The number of stars in each bin are listed above their error bars. There is a slight declining trend seen at ∼700 pc, however, we do not see a strong height/age dependence.

anism creating our observed dust populations happens randomly throughout low-mass stellar populations. We will explore possible mechanisms to create dust around old field stars in §5.

4.6. *Orion OB1 Candidate Stars*

Although the Orion complex and regions within the complex have been extensively researched (see Bally 2008, and references therein), we found seven stars that have not been previously linked to the region. All seven candidates are found within a few degrees of Orion's Belt, a neighborhood with many young star-forming regions. Specifically, these stars are possible members of the Orion OB1 association. The positions of our Orion stars are shown in Figure 20. Three of our stars fell into the Orion footprint investigated by Caballero & Solano (2008), but were not included in their sample, possibly due to their color selection criteria or depth of coverage. The majority of our Orion candidates have photometric distances between 100–340 pc, which distributes them approximately within the extent of the OB1 association ($d \sim 100$–400 pc; Caballero et al. 2007). One of our Orion candidates may be foreground or background star, based on its kinematics (§4.3). Basic information for the Orion candidates is listed in Table 12. Some of our Orion candidates showed a number of forbidden emission lines (e.g., [O I]), giving further evidence for their youth. One such star will be discussed below.

4.6.1. *Candidate 41*

One of our candidates showed up as an outlier in our SED fits (see Fig. 7). The SED fit for this star suffered from large uncertainties in both the radius and luminosity estimate, although the temperature fit was within the spread of its spectral type (2900^{+600}_{-100} K; dM4). Closer inspection of this star uncovered strong Balmer emission lines as well as a number of forbidden lines within its spectrum ([O I], [N II], and [S II]), as shown in Figure 21. Similar forbidden lines are observed in the spectrum of T Tauri stars (Appenzeller et al. 1984). Comparing the candidate spectrum to a template spectrum from Bochanski et al. (2007b) shows veiling of the photosphere; whereby additional flux, typically from accretion, weakens spectral features.

This star is also one of our Orion OB1 candidates. The Orion OB1 association is assumed to have an age between ∼8–10 Myr (Briceño et al. 2007). If we assume a temperature of 3,000 K for this star, using the isochrones from Baraffe et al. (1998, 2002) this star will have a radius of $\sim 0.8 R_\odot$, the assumed radius from our parameter fits (§3), at an age of ∼1–2 Myr. Even though there appears to be an age discrepancy, with the large uncertainties on the effective temperature and radius of this star, we cannot confidently estimate an age using isochrones. Candidate 41 is prime for follow-up observations to more accurately characterize its properties.

5. DISCUSSION

We identified 175 M dwarfs with IR excess at 12 and/or 22 μm, a typical signature of warm circumstellar material. From our youth analysis, we found that only ∼3% show reliable youth diagnostics, and we conclude that the majority of stars in our sample have ages $\gtrsim$ 1 Gyr; far older than the disk dispersal time for solar-type stars (10s of Myr; Williams & Cieza 2011). This places the majority of our sample within the older field population. Unfortunately, without strict constraints on age we are not able to inform the timescale for disk dispersal in low-mass stars under the assumption we are observing primordial dust. Candidates in close proximity of the Orion OB1 association were more likely to show signs of lithium absorption, making them potentially younger than the rest of our sample ($\lesssim$ 100 Myr). Due to their potential youth, these stars may still retain their primordial dust content. For the remaining stars, we examine possible scenarios to explain the appearance of warm dust.

The minimum distances of the dust populations, typically found within the snow line of M dwarfs, and the high fractional luminosities imply that we may be viewing dust created by planetary impacts within the terrestrial zone, similar to conclusions drawn by Weinberger et al. (2011). BD +20 307 is a spectroscopic binary composed of two F-type stars and is estimated to be older than 1 Gyr, with a large fractional IR luminosity ($L_{\rm dust}/L_* \approx 0.032$; Weinberger et al. 2011). Using a measured *Spitzer* spectrum, Weinberger et al. (2011) deduced that the most likely cause for a high fractional IR luminosity, and the crystallinity of their best-fit dust model, was a single giant impact of planetary bodies (specific incident kinetic energy of the two impacting objects $\gtrsim 10^5$ J km^{-1}).

A similar scenario has been used to explain IR excesses observed around older ($\gtrsim$ 1 Gyr) FGK stars (Rhee et al. 2008; Moór et al. 2009; Fujiwara et al. 2010; Melis et al. 2010b; Weinberger et al. 2011). Weinberger et al. (2011) argue that a fifth terrestrial planet within a planetary system such as our own could remain stable for up to a Gyr. Simulations show that the planet's orbit could have taken it across the asteroid belt, perturbing asteroids into unstable orbits, increasing the impact rate of asteroids within the inner solar system, all prior to removal from our system (Chambers 2007). This planet is also able to create collisions between terrestrial planets prior to leaving the system. This "Planet V" scenario has been used as a possible explanation for the late heavy bombardment period within our Solar system (Chambers 2007). Using numeric simulations Laskar & Gastineau

Table 12
Orion Candidate Parameters

Catalog Number	*WISE* Designation	R.A. (J2000.0) (deg)	Decl. (J2000.0) (deg)	SpT[a] ±1	RV (km s^{-1})	d[b] (pc)	Z (pc)	A_V[c] (mags)	R_V[d]
37.....	J052604.21−000220.9	81.517565	-0.039167	M5	37.6 ± 4.7	130	-27	0.41 ± 0.07	3.1
38.....	J052756.04+001459.5	81.983513	0.249883	M4	28.2 ± 4.7	152	-33	0.26 ± 0.05	5.0
39.....	J052800.30+002546.7	82.001268	0.429638	M7	41.8 ± 6.2	122	-23	0.00 ± 0.02	3.1
40.....	J053207.80+001704.9	83.032543	0.284724	M2	32.2 ± 3.8	195	-44	0.52 ± 0.02	3.1
41.....	J053215.59−003900.1	83.064987	-0.650051	M4	55.9 ± 5.5	241	-59	0.21 ± 0.07	3.1
42.....	J053311.20+001358.5	83.296678	0.232939	M3	30.8 ± 3.4	128	-23	0.35 ± 0.06	3.1
43.....	J053906.74+003722.6	84.778096	0.622946	M3	13.2 ± 2.6	331	-75	0.48 ± 0.05	3.1

[a] Determined in West et al. (2011).
[b] Photometric distances have typical uncertainties of ∼20%.
[c] Measured in Jones et al. (2011).
[d] Adopted parameters from Jones et al. (2011) measurements.

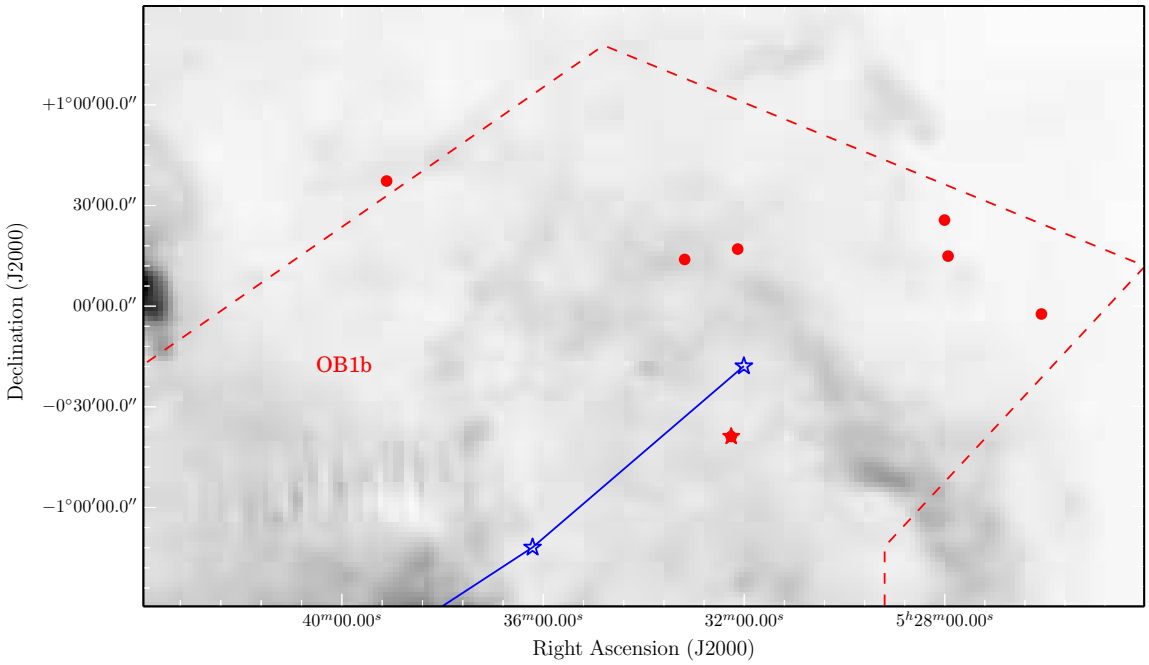

Figure 20. Orion stars (red circles) overlaid on a cutout of the *IRAS* IRIS 100 μm map (Miville-Deschênes & Lagache 2005). The approximate boundary of the OB1b subassociation is shown (red dashed line; Briceño et al. 2007). Orion's Belt is shown for reference (blue line). Candidate 41 is shown as the red star.

(2009) showed that over the course of a few Gyr, our own planetary system may become unstable and result in collisions of terrestrial planets, making this a possible scenario for terrestrial systems around M dwarfs.

In a NIR interferometric study of solar-type and higher-mass stars with debris disks undertaken by Absil et al. (2013), it was argued that collisions between large planetismals could create a significant, observable amount of dust. However, they deemed this an unlikely scenario for stars $\gtrsim$ 1 Gyr since these types of collisions are expected to happen during the final stages of planet formation ($\lesssim$ a few 100s of Myr; Chambers 2004). Clearly the timescales for such an occurrence still require further modeling to help constrain the timescale for collisions in planetary systems.

Using statistics from *Spitzer* and *IRAS*, Weinberger et al. (2011) estimate that the giant impact rate for solar-type stars is $\gtrsim$ 0.2 impacts per star during its main sequence lifetime. Following a similar argument, we can estimate the number of giant impacts for M dwarfs. The number of giant impacts per star can be estimated as $N_{\rm g} = f_* A L^{-1}$, where f_* is the fraction of stars observed to have warm dust, L is the lifetime of the collision products, and A is the age of the stars surveyed. Assuming the total number of stars we could have observed with similar fractional IR luminosities within the W11 catalog to be stars with $J \leq 17$, we are left with 41,120 stars after our cuts (see §4.5 for details). We observed 168 stars with warm dust populations that do not appear to be primordial in nature (we have omitted the Orion candidates), giving us a fraction of $f_* \approx 4.1 \times 10^{-3}$. Weinberger et al. (2011) used 100,000 years for L. This value was originally calculated by Melis et al. (2010b) for a collisional cascade started by planetary embryos with radii of ∼100 m, but was found to be similar to the 80,000 years found by Weinberger et al. (2011) for a

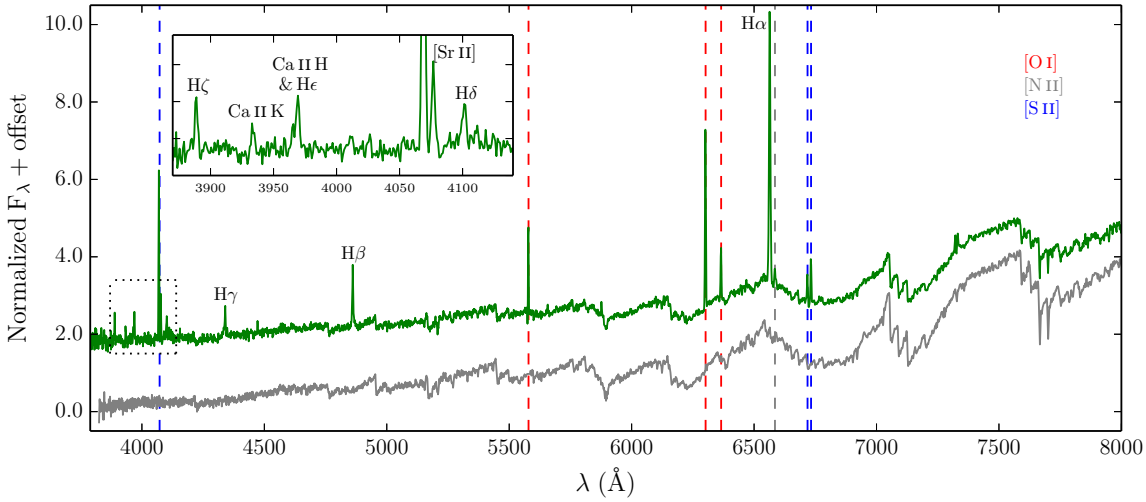

Figure 21. SDSS spectrum of candidate 41 (green line) and a template spectrum of the same spectral type from Bochanski et al. (2007b, gray line). There are a number of forbidden line transitions seen in this spectrum (line colors correspond to elements listed on the right side of the plot). These forbidden transitions are typically associated with T Tauri stars, and are an indication of accretion. The two emission lines ∼7300 Å are most likely [O II] lines (Kogure & Leung 2010). The dotted box represents the area of the inset plot. Comparing the two spectra, veiling is apparent in our candidate spectrum.

collisional cascade started from a planet-sized impact.

To estimate an average age for our observed stars, we used the activity lifetimes (i.e., the timescale during which Hα should be observable in the stellar spectrum due to magnetic activity) results of West et al. (2008). For the 41,120 stars within the W11 catalog that made our cuts, we took the total number of inactive stars within a spectral type bin and multiplied those stars by the average activity lifetime for that spectral type bin from West et al. (2008). We did the same for active stars, assuming an age of half the activity lifetime for each spectral type bin. We then took the average age across the 41,120 stars, giving us an estimated average age of $A \approx 2.6$ Gyrs. We use 2.6 Gyrs as a lower limit on the age, as many of these fields stars are likely older than 5 Gyrs, which will only increase our collision estimate. Using our estimated quantities, we find the rate at which such planetary collisions occur around M dwarfs should be $\gtrsim$ 100 impacts per star over its current age; three orders of magnitude larger than the number of impacts found by Weinberger et al. (2011) for A- through G-type stars.

A high rate of giant impacts within the terrestrial planet zone for low-mass stars has repercussions for close-in planetary systems. The high occurrence rate of terrestrial planets orbiting low-mass stars (Dressing & Charbonneau 2013; Kopparapu 2013) not only supports the possibility of this scenario, it also implies that a high rate of planetary collisions could significantly alter the habitability of such systems. N-body simulations for planet formation around low-mass stars also indicate that giant impacts could be quite common for these planetary systems (Ogihara & Ida 2009). Future simulations should attempt to constrain the timescale and frequency for such impacts to occur, and the likelihood of observing such impacts within our Galaxy. Due to the assumed ages of our stars, we find giant impacts within the terrestrial zone to be the most plausible explanation for our observed IR excesses.

To investigate whether our observed IR excesses could be due to *primordial* dust requires an evolutionary study of the fraction of M dwarfs with IR excesses at different stellar ages. Unfortunately, detection limits and small sample sizes have hindered a thorough statistical analysis for disk lifetimes. We expect low-mass stars older than a few 10s of Myr to harbor cold disk populations ($T_{\rm dust} < 100$ K), rather than the warm disks in our study. The lack of cold dust populations found around M dwarfs in contrast to debris disks found around similar age, higher-mass stars indicates that primordial warm dust should not be found around low-mass stars $\gtrsim$ 1 Gyr. However, this conclusion may be biased due to observational limits in detecting cold dust around low-mass stars. Future studies of *Spitzer* and *Herschel* data may further constrain the timescale for disk dispersal around M dwarfs.

If we consider the possibility that we are observing *primordial* dust, we can explore kinematic arguments. The primary dispersal mechanism for low-mass stars is thought to be stellar wind drag (Plavchan et al. 2005, 2009), whereby the collisionally processed grains are removed by the proton wind rather than radiation pressure. If disk kinematics are able to overcome gravitational instabilities and stellar wind drag, a star may be able to retain its primordial dust content. Studies investigating planet masses around low-mass stars indicate that there is a paucity of Jupiter- versus sub-Neptune-sized planets (Howard et al. 2012). These findings have been attributed to low disk masses from which to build planets (Laughlin et al. 2004; Kennedy & Kenyon 2008). If there is a small enough reservoir of dust, a scenario in which the collision rate within low mass disks continues to reprocess the dust while inhibiting planet formation is a possibility for low-mass stars. Studies investigating asteroids as failed planets within our Solar System lend support to this argument (Coradini et al. 2011; Sierks et al. 2011; Russell et al. 2012). The likelihood of this scenario would need to be studied through dynamical simulations to explore its plausibility.

For dust that is not primordial, we may be able to ex-

plain warm dust around older stellar populations through tidal disruption of planetary bodies. This is a phenomenon that has been observed around white dwarfs (WDs; e.g., Jura 2003, 2008; Farihi et al. 2009). Through accretion of planetary bodies, these WDs show spectral signs of heavy elements in absorption (Holberg et al. 1997). In the case of WDs, shedding of the outer layers during the transition from giant to dwarf is potentially responsible for perturbing the orbits of minor planetary bodies. No such mechanism exists for low-mass stars that have not evolved off the main sequence, making this scenario unlikely for our sample. Our estimated minimum orbital distances for our dust populations are also greater than the estimated Roche-limit for M dwarfs ($\lesssim 0.01$ AU), likely ruling out this scenario. Likewise, we can discount that our observed excesses are due to collisions fed by an asteroid belt, as dynamical models estimate much lower fractional IR luminosities than those observed (Wyatt et al. 2007).

Another possible disruption scenario involves the inherently chaotic nature of planetary orbits (Murray & Holman 1999). For close-in giant planets with unstable orbits that degrade to come within the corotation radius of their host star, it is expected that they would lose angular momentum quickly to the host star through tidal interactions. This would result in tidal disruption once the planet comes within the host star's Roche limit (Schlaufman & Winn 2013). As the material is accreted onto the host star the dust would heat up and appear as an IR excess. The dynamical arguments of Schlaufman & Winn (2013) did not include low-mass stars or Earth-sized planets, however, if we assume their arguments scale to lower-masses we find that the corotation radius for a $0.5M_{\odot}$ star is $\lesssim 0.1$ AU. Mass scaling relations for the core accretion process responsible for forming giant planets, estimate the distance of the snow-line for low-mass stars during the time of giant planet formation is > 1 AU (Laughlin et al. 2004; Adams et al. 2005; Ida & Lin 2005; Kennedy & Kenyon 2008). Due to the relative paucity of Jupiter-sized planets around low-mass stars (Johnson et al. 2007), we find it unlikely that such a migration scenario occurs at high frequency. A study investigating the likelihood of this scenario for Earth-sized planets around low-mass stars should be undertaken in the future.

To provide a separate explanation for IR excesses observed for our high-velocity stars, we consider ζ Oph, a high-mass, runaway star with a shock clearly visible in the *WISE* image archives. This star shows significant IR flux in the form of thermal emission from the bowshock of its astrosphere. Crude estimates using aperture photometry on the *WISE* images give a flux ratio of $F_{\rm star+bowshock}/F_{\rm star} > 10$ for both the $W3$ and $W4$ bands. This phenomenon has been observed around a number of runaway massive stars (Peri et al. 2012), but requires further investigation to determine if it is a viable scenario for high-velocity, low-mass stars.

6. SUMMARY

Using the West et al. (2011) SDSS catalog of 70,841 spectroscopically classified M dwarfs, we searched for IR excesses as signatures of warm circumstellar disks using *WISE* data. Applying a number of selection criteria, including our own SDSS/*WISE* color-color selection criteria using $r-z$ color as a temperature proxy, we discovered 175 stars with significant excess flux at 12 and/or 22 μm, most probably due to circumstellar material. We explored the possibility that any of our excesses could be due to an ultracool companion and found that none of our candidates exhibited flux levels representative of an ultracool companion at $\geq 3\sigma$ level. Using statistical arguments, we concluded that our observed IR excesses arising from chance alignment with extragalactic sources or Galactic cirrus contamination were unlikely.

Fitting our observational data to SEDs, we modeled both the stellar and dust components of our fits. We find that our fractional IR luminosities, $L_{\rm dust}/L_{*}$, are high ($> 10^{-3}$). These values are similar to those found around higher-mass stars showing IR excesses at ages $\gtrsim 1$ Gyr (Weinberger et al. 2011). Dust equilibrium models put our disks typically within a few tenths of an AU to their host star, and possibly closer depending upon the parameters chosen. None of our dust populations have a minimum orbital distance < 0.01 AU, the approximate Roche limit for low-mass stars, indicating that tidal disruption of planetary bodies is not a likely cause of the observed IR excess. Our estimated dust masses are slightly smaller than masses found in debris disks around higher-mass stars ($\sim 10^{-3}$–$10^{-4} M_{\rm moon}$; Chen et al. 2005), and can be attributed to lower-mass disks around lower-mass stars.

We tested our sample for youth by observing lithium absorption, measuring surface gravity tracers (CaH 3, K I, and Na I) and magnetic activity tracers (Hα, UV flux). Only a fraction of the stars in our sample ($\sim$3%) show multiple signs of youth, and we conclude that the majority of our stars are field dwarfs older than a Gyr. Seven of our candidate stars lie in the footprint of the Orion OB1 association. Most of the Orion candidate stars are magnetically active ($\sim$86%), show low surface gravity relative to the W11 catalog of M dwarfs, or show lithium absorption, and in some cases a combination of several youth tracers. Stars showing lithium absorption likely indicate an age $\lesssim 100$ Myr. Although previously unidentified, most of these stars are likely members of the OB1 association.

An analysis of UVW space motions uncovered the Orion sample to be a kinematically younger population of stars relative to our entire sample. The remainder of our candidates exhibited kinematics similar to typical disk populations, with a few high-velocity exceptions. Five stars exhibited total velocities greater than 400 km s^{-1} relative to the local standard of rest. Neither the dynamical origin of these stars, nor the mechanism to propel them to such high-velocities are known. It is possible that if these stars are moving supersonically through dense regions of the ISM, that a significant bowshock could produce high levels of IR flux, supplanting the need for a circumstellar disk to explain an IR excess.

To further investigate the timescale of this phenomenon, we employed the use of "Galactic Stratigraphy," using 12 μm excess as a disk (and hence age) proxy. We find that the disk fraction for stars as a function of vertical height from the Galactic plane remains fairly constant out to a height of $\sim$700 pc at which point the fraction begins to drop off. We do not see a significant difference for early versus late spectral types. This likely

implies there is no strong age dependence of the mechanism responsible for this phenomenon.

The estimated ages of our stars ($\gtrsim 1$ Gyr) imply that we are not observing primordial dust content. Instead, we find the most likely explanation for our IR excesses is giant impacts of terrestrial planetary bodies. This hypothesis is supported by observations of similar high-fractional IR luminosity around Solar-type stars with ages $\gtrsim 1$ Gyr (Weinberger et al. 2011). Also, the lack of observed disks around low-mass stars with ages greater than a few 10s of Myr suggests that warm primordial dust content does not persist around low-mass stars for longer than 1 Gyr. The estimated number of giant impacts per low-mass star over its main sequence lifetime, $N_{\rm g} \gtrsim 100$, indicates that such occurrences may be relatively common around low-mass stars. By enlarging our sample size with photometric M dwarfs from the latest SDSS data release (DR10; Ahn et al. 2014), we should identify thousands more such excesses around field M dwarfs. These stars will also prove important targets for the Atacama Large Millimeter Array (ALMA) and future IR missions such as the *James Webb Space Telescope* and the *Space Infrared Telescope for Cosmology and Astrophysics*.

The authors would first like to thank the anonymous referees for their extremely helpful comments which greatly improved the quality of this study. The authors would also like to thank Dan Feldman, Catherine Espaillat, Dylan Morgan, and Jan-Marie Andersen for reading this manuscript and providing helpful comments, and Saurav Dhital, Isabella Trierweiler, Lara Rangel, Chris Boyter, Dan Clemens, Jim Davenport, Kevin Covey, Alycia Weinberger, Sarah Schmidt, Tom Megeath, Christine Chen, Keivan Stassun, Jonathan Foster, Debra Fischer, Meredith Hughes, and Mark Zastrow for their helpful discussions. C.A.T. would like to acknowledge the Ford Foundation for financial support. C.A.T. thanks Gibor Basri, Geoff Marcy, and Jeff Valenti for making their radial velocity fitting code available. A.A.W acknowledges funding from NSF grants AST-1109273 and AST-1255568. A.A.W. and C.A.T. also acknowledge the support of the Research Corporation for Science Advancement's Cottrell Scholarship.

Funding for the SDSS and SDSS-II has been provided by the Alfred P. Sloan Foundation, the Participating Institutions, the National Science Foundation, the U.S. Department of Energy, the National Aeronautics and Space Administration, the Japanese Monbukagakusho, the Max Planck Society, and the Higher Education Funding Council for England. The SDSS Web Site is http://www.sdss.org/. The SDSS is managed by the Astrophysical Research Consortium for the Participating Institutions. The Participating Institutions are the American Museum of Natural History, Astrophysical Institute Potsdam, University of Basel, University of Cambridge, Case Western Reserve University, University of Chicago, Drexel University, Fermilab, the Institute for Advanced Study, the Japan Participation Group, Johns Hopkins University, the Joint Institute for Nuclear Astrophysics, the Kavli Institute for Particle Astrophysics and Cosmology, the Korean Scientist Group, the Chinese Academy of Sciences (LAMOST), Los Alamos National Laboratory, the Max-Planck-Institute for Astronomy (MPIA), the Max-Planck-Institute for Astrophysics (MPA), New Mexico State University, Ohio State University, University of Pittsburgh, University of Portsmouth, Princeton University, the United States Naval Observatory, and the University of Washington.

This publication makes use of data products from the Two Micron All Sky Survey, which is a joint project of the University of Massachusetts and the Infrared Processing and Analysis Center/California Institute of Technology, funded by the National Aeronautics and Space Administration and the National Science Foundation. This publication also makes use of data products from the *Wide-field Infrared Survey Explorer*, which is a joint project of the University of California, Los Angeles, and the Jet Propulsion Laboratory/California Institute of Technology, funded by the National Aeronautics and Space Administration.

This research made use of Montage, funded by the National Aeronautics and Space Administration's Earth Science Technology Office, Computation Technologies Project, under Cooperative Agreement Number NCC5-626 between NASA and the California Institute of Technology. Montage is maintained by the NASA/IPAC Infrared Science Archive. This research also made use of Astropy, a community-developed core Python package for Astronomy (Astropy Collaboration et al. 2013). Figures in this work were created using the Python based graphics environment Matplotlib (Hunter 2007).

REFERENCES

Abazajian, K. N., Adelman-McCarthy, J. K., Agüeros, M. A., et al. 2009, ApJS, 182, 543
Absil, O., Defrère, D., Coudé du Foresto, V., et al. 2013, A&A, 555, A104
Acke, B., Min, M., Dominik, C., et al. 2012, A&A, 540, A125
Adams, F. C., Bodenheimer, P., & Laughlin, G. 2005, Astronomische Nachrichten, 326, 913
Ahn, C. P., Alexandroff, R., Allende Prieto, C., et al. 2014, ApJS, 211, 17
Allard, F., Hauschildt, P. H., Alexander, D. R., Tamanai, A., & Schweitzer, A. 2001, ApJ, 556, 357
Allard, F., Homeier, D., & Freytag, B. 2012a, Royal Society of London Philosophical Transactions Series A, 370, 2765
Allard, F., Homeier, D., Freytag, B., & Sharp, C. M. 2012b, in EAS Publications Series, Vol. 57, EAS Publications Series, ed. C. Reylé, C. Charbonnel, & M. Schultheis, 3–43
Appenzeller, I., Oestreicher, R., & Jankovics, I. 1984, A&A, 141, 108
Astropy Collaboration, Robitaille, T. P., Tollerud, E. J., et al. 2013, A&A, 558, A33
Aumann, H. H., Beichman, C. A., Gillett, F. C., et al. 1984, ApJ, 278, L23
Avenhaus, H., Schmid, H. M., & Meyer, M. R. 2012, A&A, 548, A105
Bally, J. 2008, Overview of the Orion Complex (Handbook of Star Forming Regions, Volume I), 459
Baraffe, I., & Chabrier, G. 2010, A&A, 521, A44
Baraffe, I., Chabrier, G., Allard, F., & Hauschildt, P. H. 1998, A&A, 337, 403
—. 2002, A&A, 382, 563
Baraffe, I., Chabrier, G., Barman, T. S., Allard, F., & Hauschildt, P. H. 2003, A&A, 402, 701
Beichman, C. A., Bryden, G., Rieke, G. H., et al. 2005, ApJ, 622, 1160
Bertin, E., & Arnouts, S. 1996, A&AS, 117, 393
Bessell, M. S., & Brett, J. M. 1988, PASP, 100, 1134
Binney, J., Gerhard, O., & Spergel, D. 1997, MNRAS, 288, 365
Bochanski, J. J., Hawley, S. L., Covey, K. R., et al. 2010, AJ, 139, 2679

Bochanski, J. J., Hawley, S. L., & West, A. A. 2011, AJ, 141, 98
Bochanski, J. J., Munn, J. A., Hawley, S. L., et al. 2007a, AJ, 134, 2418
Bochanski, J. J., West, A. A., Hawley, S. L., & Covey, K. R. 2007b, AJ, 133, 531
Bochanski, Jr., J. J. 2008, PhD thesis, University of Washington
Boggess, N. W., Mather, J. C., Weiss, R., et al. 1992, ApJ, 397, 420
Bonfils, X., Delfosse, X., Udry, S., et al. 2005, A&A, 442, 635
Boss, A. P. 2006, ApJ, 643, 501
Briceño, C., Hartmann, L., Hernández, J., et al. 2007, ApJ, 661, 1119
Buchhave, L. A., Latham, D. W., Johansen, A., et al. 2012, Nature, 486, 375
Burgasser, A. J., Luk, C., Dhital, S., et al. 2012, ApJ, 757, 110
Burrows, A., Marley, M., Hubbard, W. B., et al. 1997, ApJ, 491, 856
Caballero, J. A., & Solano, E. 2008, A&A, 485, 931
Caballero, J. A., Béjar, V. J. S., Rebolo, R., et al. 2007, A&A, 470, 903
Cargile, P. A., James, D. J., & Jeffries, R. D. 2010, ApJ, 725, L111
Carpenter, J. M., Mamajek, E. E., Hillenbrand, L. A., & Meyer, M. R. 2006, ApJ, 651, L49
—. 2009, ApJ, 705, 1646
Chabrier, G., & Baraffe, I. 1997, A&A, 327, 1039
Chambers, J. E. 2004, Earth and Planetary Science Letters, 223, 241
—. 2007, Icarus, 189, 386
Chen, C. H., Patten, B. M., Werner, M. W., et al. 2005, ApJ, 634, 1372
Cieza, L., Padgett, D. L., Stapelfeldt, K. R., et al. 2007, ApJ, 667, 308
Cohen, M. 1995, ApJ, 444, 874
Cohen, M., Wheaton, W. A., & Megeath, S. T. 2003, AJ, 126, 1090
Coradini, A., Capaccioni, F., Erard, S., et al. 2011, Science, 334, 492
Covey, K. R., Ivezić, Ž., Schlegel, D., et al. 2007, AJ, 134, 2398
Dawson, P., Scholz, A., Ray, T. P., et al. 2012, MNRAS, 310
Dhital, S., West, A. A., Stassun, K. G., et al. 2012, AJ, 143, 67
Doi, M., Tanaka, M., Fukugita, M., et al. 2010, AJ, 139, 1628
Dressing, C. D., & Charbonneau, D. 2013, ApJ, 767, 95
Eggen, O. J. 1990, PASP, 102, 166
Eiroa, C., Fedele, D., Maldonado, J., et al. 2010, A&A, 518, L131
Eiroa, C., Marshall, J. P., Mora, A., et al. 2011, A&A, 536, L4
—. 2013, A&A, 555, A11
Ertel, S., Wolf, S., Marshall, J. P., et al. 2012, A&A, 541, A148
Espaillat, C., Calvet, N., D'Alessio, P., et al. 2007, ApJ, 670, L135
Espaillat, C., Furlan, E., D'Alessio, P., et al. 2011, ApJ, 728, 49
Espaillat, C., Muzerolle, J., Najita, J., et al. 2014, arXiv:1402.7103
Farihi, J., Jura, M., & Zuckerman, B. 2009, ApJ, 694, 805
Fazio, G. G., Hora, J. L., Allen, L. E., et al. 2004, ApJS, 154, 10
Findeisen, K., & Hillenbrand, L. 2010, AJ, 139, 1338
Fiorucci, M., & Munari, U. 2003, A&A, 401, 781
Fischer, D. A., & Valenti, J. 2005, ApJ, 622, 1102
Fitzpatrick, E. L. 1999, PASP, 111, 63
Forbrich, J., Lada, C. J., Muench, A. A., & Teixeira, P. S. 2008, ApJ, 687, 1107
Foreman-Mackey, D., Hogg, D. W., Lang, D., & Goodman, J. 2013, PASP, 125, 306
France, K., Linsky, J. L., Tian, F., Froning, C. S., & Roberge, A. 2012, ApJ, 750, L32
Fuchs, B., Dettbarn, C., Rix, H.-W., et al. 2009, AJ, 137, 4149
Fujiwara, H., Onaka, T., Ishihara, D., et al. 2010, ApJ, 714, L152
Gáspár, A., & Rieke, G. H. 2014, ApJ, 784, 33
Gautier, III, T. N., Rebull, L. M., Stapelfeldt, K. R., & Mainzer, A. 2008, ApJ, 683, 813
Gonzalez, G. 1997, MNRAS, 285, 403
Goodman, J., & Weare, J. 2010, Communications in Applied Mathematics and Computational Science, 5, 65
Greaves, J. S. 2010, MNRAS, 409, L44
Hartmann, L. 1998, Accretion Processes in Star Formation (Cambridge, UK ; New York : Cambridge University Press, 1998. (Cambridge astrophysics series ; 32) ISBN 0521435072)
Hauschildt, P. H., Allard, F., & Baron, E. 1999, ApJ, 512, 377
Hawley, S., Reid, I. N., & Gizis, J. 2000, in Astronomical Society of the Pacific Conference Series, Vol. 212, From Giant Planets to Cool Stars, ed. C. A. Griffith & M. S. Marley, 252
Hawley, S. L., Gizis, J. E., & Reid, I. N. 1996, AJ, 112, 2799
Hawley, S. L., Covey, K. R., Knapp, G. R., et al. 2002, AJ, 123, 3409
Heng, K., & Malik, M. 2013, MNRAS
Henry, T. J., Jao, W.-C., Subasavage, J. P., et al. 2006, AJ, 132, 2360
Holberg, J. B., Barstow, M. A., & Green, E. M. 1997, ApJ, 474, L127
Howard, A. W., Marcy, G. W., Bryson, S. T., et al. 2012, ApJS, 201, 15
Huchra, J. P., & Geller, M. J. 1982, ApJ, 257, 423
Hunter, J. D. 2007, Computing in Science and Engineering, 9, 90
Ida, S., & Lin, D. N. C. 2005, ApJ, 626, 1045
Indebetouw, R., Mathis, J. S., Babler, B. L., et al. 2005, ApJ, 619, 931
Jao, W.-C., Henry, T. J., Subasavage, J. P., et al. 2005, AJ, 129, 1954
Johnson, D. R. H., & Soderblom, D. R. 1987, AJ, 93, 864
Johnson, J. A., Aller, K. M., Howard, A. W., & Crepp, J. R. 2010, PASP, 122, 905
Johnson, J. A., & Apps, K. 2009, ApJ, 699, 933
Johnson, J. A., Butler, R. P., Marcy, G. W., et al. 2007, ApJ, 670, 833
Jones, D. O., West, A. A., & Foster, J. B. 2011, AJ, 142, 44
Jura, M. 2003, ApJ, 584, L91
—. 2008, AJ, 135, 1785
Jura, M., Malkan, M., White, R., et al. 1998, ApJ, 505, 897
Kennedy, G. M., & Kenyon, S. J. 2008, ApJ, 673, 502
—. 2009, ApJ, 695, 1210
Kennedy, G. M., & Wyatt, M. C. 2012, MNRAS, 426, 91
Kerr, F. J., & Lynden-Bell, D. 1986, MNRAS, 221, 1023
Kilic, M., Munn, J. A., Harris, H. C., et al. 2006, AJ, 131, 582
Kirkpatrick, J. D., Cushing, M. C., Gelino, C. R., et al. 2011, ApJS, 197, 19
Kogure, T., & Leung, K.-C. 2010, The astrophysics of emission-line stars, Vol. 342 (Springer)
Kopparapu, R. K. 2013, ApJ, 767, L8
Krivov, A. V., Eiroa, C., Löhne, T., et al. 2013, ApJ, 772, 32
Lada, C. J. 1987, in IAU Symposium, Vol. 115, Star Forming Regions, ed. M. Peimbert & J. Jugaku, 1–17
Lada, C. J., Muench, A. A., Luhman, K. L., et al. 2006, AJ, 131, 1574
Lallement, R., Welsh, B. Y., Vergely, J. L., Crifo, F., & Sfeir, D. 2003, A&A, 411, 447
Laskar, J., & Gastineau, M. 2009, Nature, 459, 817
Laughlin, G., Bodenheimer, P., & Adams, F. C. 1997, ApJ, 482, 420
—. 2004, ApJ, 612, L73
Laws, C., Gonzalez, G., Walker, K. M., et al. 2003, AJ, 125, 2664
Lee, H.-T., & Lim, J. 2008, ApJ, 679, 1352
Leggett, S. K. 1992, ApJS, 82, 351
Lépine, S., Rich, R. M., & Shara, M. M. 2007, ApJ, 669, 1235
Lépine, S., & Shara, M. M. 2005, AJ, 129, 1483
Linsky, J., Redfield, S., Ayres, T., Brown, A., & Harper, G. 2001, in Astronomical Society of the Pacific Conference Series, Vol. 242, Eta Carinae and Other Mysterious Stars: The Hidden Opportunities of Emission Spectroscopy, ed. T. R. Gull, S. Johannson, & K. Davidson, 247
Luhman, K. L. 2004, ApJ, 602, 816
Luhman, K. L., Allen, P. R., Espaillat, C., Hartmann, L., & Calvet, N. 2010, ApJS, 186, 111
Luhman, K. L., Stauffer, J. R., Muench, A. A., et al. 2003, ApJ, 593, 1093
Luhman, K. L., Allen, L. E., Allen, P. R., et al. 2008, ApJ, 675, 1375
Lyo, A.-R., Lawson, W. A., Feigelson, E. D., & Crause, L. A. 2004, MNRAS, 347, 246
Mainzer, A., Bauer, J., Grav, T., et al. 2011, ApJ, 731, 53
Mamajek, E. E., Lawson, W. A., & Feigelson, E. D. 2000, ApJ, 544, 356
Mann, A. W., Brewer, J. M., Gaidos, E., Lépine, S., & Hilton, E. J. 2013, AJ, 145, 52
Mann, A. W., Gaidos, E., Lépine, S., & Hilton, E. J. 2012, ApJ, 753, 90

Martin, D. C., Fanson, J., Schiminovich, D., et al. 2005, ApJ, 619, L1
Mayor, M., Marmier, M., Lovis, C., et al. 2011, ArXiv e-prints
McClure, M. 2009, ApJ, 693, L81
Melis, C., Gielen, C., Chen, C. H., et al. 2010a, ApJ, 724, 470
Melis, C., Zuckerman, B., Rhee, J. H., & Song, I. 2010b, ApJ, 717, L57
Melis, C., Zuckerman, B., Song, I., Rhee, J. H., & Metchev, S. 2009, ApJ, 696, 1964
Miville-Deschênes, M.-A., & Lagache, G. 2005, ApJS, 157, 302
Mohanty, S., & Basri, G. 2003, ApJ, 583, 451
Mohanty, S., Stassun, K. G., & Doppmann, G. W. 2010, ApJ, 722, 1138
Monet, D. G., Levine, S. E., Canzian, B., et al. 2003, AJ, 125, 984
Moór, A., Apai, D., Pascucci, I., et al. 2009, ApJ, 700, L25
Morgan, D. P., West, A. A., Garcés, A., et al. 2012, AJ, 144, 93
Moro, D., & Munari, U. 2000, A&AS, 147, 361
Munn, J. A., Monet, D. G., Levine, S. E., et al. 2004, AJ, 127, 3034
—. 2008, AJ, 136, 895
Murakami, H., Baba, H., Barthel, P., et al. 2007, PASJ, 59, 369
Murray, N., & Holman, M. 1999, Science, 283, 1877
Neugebauer, G., Habing, H. J., van Duinen, R., et al. 1984, ApJ, 278, L1
Newton, E. R., Charbonneau, D., Irwin, J., et al. 2014, AJ, 147, 20
Ng, Y. K., Bertelli, G., Chiosi, C., & Bressan, A. 1997, A&A, 324, 65
Ogihara, M., & Ida, S. 2009, ApJ, 699, 824
Önehag, A., Heiter, U., Gustafsson, B., et al. 2012, A&A, 542, A33
Padgett, D. L., Cieza, L., Stapelfeldt, K. R., et al. 2006, ApJ, 645, 1283
Palladino, L. E., Schlesinger, K. J., Holley-Bockelmann, K., et al. 2014, ApJ, 780, 7
Pâris, I., Petitjean, P., Aubourg, É., et al. 2014, A&A, 563, A54
Perets, H. B. 2010, ArXiv e-prints
Peri, C. S., Benaglia, P., Brookes, D. P., Stevens, I. R., & Isequilla, N. L. 2012, A&A, 538, A108
Piffl, T., Scannapieco, C., Binney, J., et al. 2014, A&A, 562, A91
Pilbratt, G. L., Riedinger, J. R., Passvogel, T., et al. 2010, A&A, 518, L1
Pinsonneault, M. 1997, ARA&A, 35, 557
Plavchan, P., Jura, M., & Lipscy, S. J. 2005, ApJ, 631, 1161
Plavchan, P., Werner, M. W., Chen, C. H., et al. 2009, ApJ, 698, 1068
Pollack, J. B., Hollenbach, D., Beckwith, S., et al. 1994, ApJ, 421, 615
Rebull, L. M., Stapelfeldt, K. R., Werner, M. W., et al. 2008, ApJ, 681, 1484
Reid, I. N., Cruz, K. L., & Allen, P. R. 2007, AJ, 133, 2825
Reid, I. N., & Gizis, J. E. 1997, AJ, 113, 2246
Reid, I. N., & Hawley, S. L. 2005, New Light on Dark Stars : Red Dwarfs, Low-Mass Stars, Brown Dwarfs (Springer)
Reid, I. N., Hawley, S. L., & Gizis, J. E. 1995, AJ, 110, 1838
Reid, I. N., Cruz, K. L., Allen, P., et al. 2004, AJ, 128, 463
Reiners, A., & Basri, G. 2008, ApJ, 684, 1390
Rhee, J. H., Song, I., & Zuckerman, B. 2008, ApJ, 675, 777
Roeser, S., Demleitner, M., & Schilbach, E. 2010, AJ, 139, 2440
Rojas-Ayala, B., Covey, K. R., Muirhead, P. S., & Lloyd, J. P. 2010, ApJ, 720, L113
—. 2012, ApJ, 748, 93
Rojas-Ayala, B., & Lloyd, J. P. 2010, in Astronomical Society of the Pacific Conference Series, Vol. 430, Pathways Towards Habitable Planets, ed. V. Coudé Du Foresto, D. M. Gelino, & I. Ribas, 528
Russell, C. T., Raymond, C. A., Coradini, A., et al. 2012, Science, 336, 684
Salim, S., & Gould, A. 2003, ApJ, 582, 1011
Schlaufman, K. C., & Laughlin, G. 2010, A&A, 519, A105
Schlaufman, K. C., & Winn, J. N. 2013, ApJ, 772, 143
Schlegel, D. J., Finkbeiner, D. P., & Davis, M. 1998, ApJ, 500, 525
Schlieder, J. E., Lépine, S., Rice, E., et al. 2012a, AJ, 143, 114
Schlieder, J. E., Lépine, S., & Simon, M. 2012b, AJ, 143, 80
Schmidt, S. J., West, A. A., Hawley, S. L., & Pineda, J. S. 2010, AJ, 139, 1808
Schönrich, R., Binney, J., & Dehnen, W. 2010, MNRAS, 403, 1829
Shkolnik, E., Liu, M. C., & Reid, I. N. 2009, ApJ, 699, 649
Shkolnik, E. L., Anglada-Escudé, G., Liu, M. C., et al. 2012, ApJ, 758, 56
Shkolnik, E. L., Liu, M. C., Reid, I. N., Dupuy, T., & Weinberger, A. J. 2011, ApJ, 727, 6
Sierks, H., Lamy, P., Barbieri, C., et al. 2011, Science, 334, 487
Skrutskie, M. F., Cutri, R. M., Stiening, R., et al. 2006, AJ, 131, 1163
Skumanich, A. 1972, ApJ, 171, 565
Slesnick, C. L., Carpenter, J. M., & Hillenbrand, L. A. 2006, AJ, 131, 3016
Soderblom, D. R., Duncan, D. K., & Johnson, D. R. H. 1991, ApJ, 375, 722
Song, I., Weinberger, A. J., Becklin, E. E., Zuckerman, B., & Chen, C. 2002, AJ, 124, 514
Strömberg, G. 1922, ApJ, 56, 265
—. 1925, ApJ, 61, 363
Su, K. Y. L., Rieke, G. H., Misselt, K. A., et al. 2005, ApJ, 628, 487
Swift, D. C., Eggert, J. H., Hicks, D. G., et al. 2012, ApJ, 744, 59
Terrien, R. C., Mahadevan, S., Bender, C. F., et al. 2012, ApJ, 747, L38
Walkowicz, L. M., Johns-Krull, C. M., & Hawley, S. L. 2008, ApJ, 677, 593
Warren, Jr., W. H., & Hesser, J. E. 1977, ApJS, 34, 115
Weinberger, A. J., Becklin, E. E., Song, I., & Zuckerman, B. 2011, ApJ, 726, 72
Weinberger, A. J., Becklin, E. E., Zuckerman, B., & Song, I. 2004, AJ, 127, 2246
Werner, M. W., Roellig, T. L., Low, F. J., et al. 2004, ApJS, 154, 1
West, A. A., & Basri, G. 2009, ApJ, 693, 1283
West, A. A., Hawley, S. L., Bochanski, J. J., et al. 2008, AJ, 135, 785
West, A. A., Morgan, D. P., Bochanski, J. J., et al. 2011, AJ, 141, 97
White, R. J., & Basri, G. 2003, ApJ, 582, 1109
Williams, J. P., & Cieza, L. A. 2011, ARA&A, 49, 67
Wilner, D. J., Andrews, S. M., MacGregor, M. A., & Hughes, A. M. 2012, ApJ, 749, L27
Wilson, O. C. 1963, ApJ, 138, 832
Woolf, V. M., & Wallerstein, G. 2006, PASP, 118, 218
Wright, E. L., Eisenhardt, P. R. M., Mainzer, A. K., et al. 2010, AJ, 140, 1868
Wyatt, M. C., Smith, R., Greaves, J. S., et al. 2007, ApJ, 658, 569
Yan, L., Donoso, E., Tsai, C.-W., et al. 2013, AJ, 145, 55
Yasui, C., Kobayashi, N., Tokunaga, A. T., Saito, M., & Tokoku, C. 2009, ApJ, 705, 54
—. 2010, ApJ, 723, L113
York, D. G., Adelman, J., Anderson, Jr., J. E., et al. 2000, AJ, 120, 1579
Zuckerman, B. 2001, ARA&A, 39, 549